High-resolution observations and modeling of turbulence sources, structures, and intensities in the upper mesosphere

David C Fritts, Ling Wang, Gerd Baumgarten, Amber Miller, Marvin A Geller, Glenn Jones, Michele Limon, Daniel Chapman, Joy Didier, Carl B Kjellstrand, et al.

High-Resolution Observations and Modeling of Turbulence Sources, Structures, and Intensities in the Upper Mesosphere

David C. Fritts[1], Ling Wang[1], Gerd Baumgarten[2], Amber D. Miller[3], Marvin A. Geller[1], Glenn Jones[3], Michele Limon[3], Daniel Chapman[3], Joy Didier[3], Carl B. Kjellstrand[3], Derek Araujo[3], Seth Hillbrand[4], Andrei Korotkov[5], Gregory Tucker[5], and Jerry Vinokurov[5]

[1]GATS Inc., Boulder Division, Boulder, CO

[2]Leibniz Institute for Atmospheric Physics, Kühlungsborn, DE

[3]Department of Physics, Columbia University, New York, NY

[4]Department of Physics and Astronomy, California State University, Sacramento, CA

[5]Department of Physics, Brown University, Providence, RI

Corresponding author: D. C. Fritts

Address: GATS Inc., 3360 Mitchell Lane, Boulder, CO 80301

Email: dave@gats-inc.com

Phone: 720-274-4747

Submitted to Journal of Atmospheric and Solar-Terrestrial Physics

1 June 2016

Abstract

New capabilities for imaging small-scale instabilities and turbulence and for modeling gravity wave (GW), instability, and turbulence dynamics at high Reynolds numbers are employed to identify the major instabilities and quantify turbulence intensities near the summer mesopause. High-resolution imaging of polar mesospheric clouds (PMCs) reveal a range of instability dynamics and turbulence sources that have their roots in multi-scale GW dynamics at larger spatial scales. Direct numerical simulations (DNS) of these dynamics exhibit a range of instability types that closely resemble instabilities and turbulence seen in PMC imaging and by ground-based and *in-situ* instruments at all times and altitudes. The DNS also exhibit the development of "sheet-and-layer" (S&L) structures in the horizontal wind and thermal stability fields that resemble observed flows near the mesopause and at lower altitudes.

Both observations and modeling suggest major roles for GW breaking, Kelvin-Helmholtz instabilities (KHI), and intrusions in turbulence generation and energy dissipation. Of these, larger-scale GW breaking and KHI play the major roles in energetic flows leading to strong turbulence. GW propagation and breaking can span several S&L features and induce KHI ranging from GW to turbulence scales. Intrusions make comparable contributions to turbulence generation as instabilities become weaker and more intermittent. Turbulence intensities are highly variable in the vertical and typically span 3 or more decades. DNS results that closely resemble observed flows suggest a range of mechanical energy dissipation rates of $\varepsilon \sim 10^{-3}$-10 Wkg^{-1} that is consistent with the range of *in-situ* measurements at ~80-90 km in summer.

Key Words: polar mesospheric clouds, gravity waves and instabilities, turbulence, MLT dynamics

1. Introduction

Turbulence has been recognized to be a ubiquitous component of the motion spectrum throughout the atmosphere for more than five decades (e.g., Panofsky, 1959; Blamont and DeJager, 1961; Obukhov, 1962; Witt, 1962; Lumley and Panofsky, 1964; Rees et al., 1972; Woodman and Guillen, 1974; Zimmerman et al., 1977; Lilly, 1983; Wyngaard, 1992, 2010; Gibson, 1996; and references therein). At all altitudes below the turbopause at ~105-110 km, above which kinematic viscosity and thermal diffusivity largely suppress turbulence sources, turbulence is believed to play multiple roles. In the mesosphere and lower thermosphere (MLT), direct turbulence effects include 1) heating due to turbulence dissipation (Hocking, 1985; Lübken, 1997; Becker and Schmitz, 2002; Lübken et al., 2002) and 2) mixing and transports of heat, momentum, and constituents (e.g., Weinstock, 1978a, b; Schoeberl and Strobel, 1983; Chao and Schoeberl, 1983; Fritts and Alexander, 2003, hereafter FA03; Bishop et al., 2004; Rapp et al., 2004; Hecht et al., 2004). Importantly, however, the efficiency of turbulent transports remains uncertain and strongly debated (Fritts and Dunkerton, 1985; Coy and Fritts, 1988; Strobel et al., 1987; McIntyre, 1989; Becker and Schmitz, 2002; Becker and McLandress, 2009). Turbulence also contributes indirectly to 3) the dissipation of, and heat and momentum deposition by, gravity waves (GWs) and larger-scale motions (Hodges, 1967; Lindzen, 1981; Walterscheid, 1981; Holton, 1982; Garcia and Solomon, 1987; FA03; Medvedev and Klaassen, 2003; Yigit, 2015) and 4) the generation of GWs accompanying larger-scale inhomogeneities in turbulence layers (Dohan and Sutherland, 2005).

The importance of turbulence in the MLT derives from the various motions that contribute to local instabilities at these altitudes. The large majority of the wind shear variance in the MLT is due to propagation of GWs, tides, and planetary waves (PWs) from sources at lower altitudes, and to their superpositions and interactions in the MLT accompanying their amplitude increases with altitude. Of these motions, GWs contribute the major energy and momentum fluxes because of their much larger vertical group velocities (FA03). GW interactions with the larger-scale motions, and other GWs, cause refraction to smaller vertical scales, amplitude increases, instabilities, and dissipation, resulting in only ~0.1% of the GW energy generated in the troposphere reaching altitudes of ~80-90 km (Fritts and VanZandt, 1993, hereafter FV93). Despite this severe dissipation, GW velocity variances are ~2 decades larger near the mesopause than near the tropopause (Balsley and Carter, 1982; Balsley and Garello, 1985) and mechanical energy dissipation rates in the mesosphere, typically $\varepsilon \sim 10^{-3}$-1 Wkg^{-1}, are similarly ~2 decades larger than in the troposphere and lower stratosphere under stable conditions (Lawrence and Balsley, 2013; Schneider et al., 2014; Fritts et al., 2016, hereafter F16).

High-resolution observations at multiple altitudes suggest that the dynamics accounting for systematic GW energy dissipation, and energy and momentum deposition, often involve "sheet-and-layer" (S&L) structures comprising thinner, strongly stratified and sheared sheets and thicker, weakly stratified and sheared layers (e.g., Gossard et al. 1985; Dalaudier et al. 1994; Coulman et al. 1995; Luce et al. 1995, 1999; Balsley et al. 1998, 2003, 2012; Muschinski and Wode 1998; Nastrom and Eaton 2001; Fritts et al., 2004, hereafter F04; Rapp et al., 2004; Chuda et al. 2007; Clayson and Kantha, 2008). High-resolution direct numerical simulations (DNS) reveal that such S&L structures arise naturally from superposed and interacting GWs and larger-scale winds having various spatial and temporal scales (Fritts et al., 2013, 2016; Fritts and Wang, 2013; hereafter F13, F16, and FW13, respectively). Both observations and DNS modeling reveal that S&L structures tend to exhibit the strongest potential temperature and horizontal wind gradients, $d\theta/dz$ and du/dz, up to ~10 times the mean gradients or larger, during the most active instabilities and strongest turbulence. These decay with time in the absence of continued energy inputs, but they can nevertheless extend for 10's of buoyancy periods (FW13; F16). Though studied independently, these same dynamics also play major roles in oceans and lakes (e.g., Osborn and Cox, 1972; Gregg, 1975; Thorpe, 1977, 2005; Osborn, 1980; Dillon, 1982; Wesson and Gregg, 1994; Moum, 1996; Ferron et al., 1998; Gargett, 1999).

Recent DNS modeling has suggested that the "multi-scale dynamics" (MSD) that drive S&L structures and evolutions comprise superposed and interacting GWs and larger-scale flows, sporadic instabilities of several types, and sporadic turbulence events (F13; F16). The major instabilities accompanying MSD include GW breaking, Kelvin-Helmholtz instabilities (KHI), and intrusions, and these can have very different influences on S&L evolutions.

GW breaking within MSD occurs on scales comparable to and deeper than local S&L scales, and leads to turbulence and mixing largely within the weakly-stratified layers. GWs also enhance the potential for KHI, both in the absence of, and accompanying, breaking. Hence, GW breaking and KHI often occur together or in close proximity. However, KHI occurs only on more strongly stratified and sheared sheets because the shears that enable KHI can only be sustained in high stratification. Sufficiently strong KHI can also lead to splitting of the initial sheet, as observed by Woods and Wiley (1972) in the ocean and modeled earlier with high-resolution DNS or large-eddy simulation (e.g., Werne and Fritts, 1999; Fritts et al., 2012; hereafter WF99 and F12, respectively). When the MSD flows are energetic, e.g., a buoyancy Reynolds number $Re_b=\varepsilon/\nu N_0^2>20$ (Smyth and Moum, 2000), where ν and N_0 are kinematic viscosity and the mean buoyancy frequency, GW breaking and KHI predominate and the nearly laminar sheets have strong stratification and shear. As MSD become less energetic, intrusions compete with smaller-scale GW breaking, turbulence events are weaker, and the underlying GWs no longer contribute the strong shearing needed to maintain strongly stratified and sheared sheets (F16).

While considerable observational evidence for MSD has come from the lower atmosphere and oceans, multiple stratospheric and MLT observations have also revealed apparent S&L structures and/or instability dynamics that are suggestive of MSD. Evidence of layering and multi-scale spatial and temporal variability in temperatures, winds, tracers, and/or turbulence intensities includes the following:

1) high-resolution balloon observations (Barat, 1982; Dalaudier et al., 1994; Gavrilov et al., 2005; Clayson and Kantha, 2008; Schneider et al., 2014),
2) MF, VHF, and UHF radar measurements of radar backscatter and/or spectral widths in the stratosphere and mesosphere (Woodman and Guillen, 1974; Sato and Woodman, 1982; Gage and Balsley, 1984; Hocking, 1985; Luce et al., 1995, 2006), and

3) in-situ rocket and falling-sphere measurements (Lübken, 1997; Lübken et al., 2002; Rapp et al., 2004; Goldberg et al., 2006; Lehmacher et al., 2011; Szewczyk et al., 2013).

Additional evidence of instability dynamics suggestive of MSD influences and/or specific instability forms seen in airglow, polar mesospheric clouds (PMCs, also referred to as noctilucent clouds when viewed from below), chemical release imaging, and/or new DNS modeling includes the following:

4) localized GW enhancements, breaking, and/or instabilities (Yamada et al., 2001; Fritts et al., 2002, 2014a, hereafter F14a; Bossert et al., 2015),
5) localized KHI, several at peak GW vertical displacements, or along their descending phases (Witt, 1962; Fritts and Rastogi, 1985; Hecht, 2004; Hecht et al., 2005, 2014; Lehmacher et al., 2007; Pfrommer et al., 2009; Baumgarten and Fritts, 2014, hereafter BF14; Fritts et al., 2014b, c, hereafter F14b and F14c),
6) potential deep convective rolls (Larsen, 2000; Larsen et al., 2004), and
7) apparent intrusions of turbulent air into quiescent air seen in high-resolution PMC imaging (Miller et al., 2015, hereafter M15).

Thus, there is significant evidence for fairly ubiquitous MSD and S&L features at all altitudes from the surface to ~100 km. This is not a universal characterization of atmospheric or MLT instability dynamics, however, as there is also evidence of more idealized instability dynamics accompanying large-amplitude, nearly-monochromatic or superposed GWs having vertical wavelengths larger than S&L vertical scales. Importantly, larger vertical wavelengths and intrinsic phase speeds may allow such GWs to contribute to MSD at lower altitudes and amplitudes, and also attain larger amplitudes and rapid instability evolution without strong influences by smaller-scale S&L features at higher altitudes. Examples include the following:

1) idealized GW and KHI dynamics predicted by theory and singular vector analysis and identified by DNS, such as GW breaking fronts, streamwise-aligned vortices, vortex rings, and KHI secondary instabilities observed in PMC and airglow imaging to date

(e.g., Achatz, 2005, 2007; F09a; F09b; Fruman and Achatz 2012; F13; Remmler et al. 2013; BF14; F14b; F14c; Fruman et al., 2014; Hecht et al., 2014; M15), and

2) nonlinear dynamics comprising various wave-wave and wave/mean-flow interactions, including "self-acceleration" (SA) dynamics, modulational instabilities, and overturning of localized GW packets at large amplitudes and/or intrinsic frequencies (Sutherland, 2001, 2006a, 2006b; Doser and Sutherland, 2011; Fritts et al., 2015, hereafter F15),

Summarizing, various analysis and modeling methodologies are now providing important insights into the various instability dynamics contributing to GW dissipation and turbulence production throughout the atmosphere. DNS, in particular, is identifying specific instability features at finite amplitude that resemble those observed by high-resolution imaging in the MLT.

Our goals in this paper are to explore the ability of high-resolution DNS to describe realistic GW and MSD instability and turbulence events and aid in the interpretation of observed events in the MLT. To achieve these goals, our efforts will include three components:

1) employ ground-based and balloon-borne PMC imaging to identify the types, scales, and stages of instability dynamics accounting for MLT turbulence,
2) use these results to select and scale DNS of idealized GW breaking and MSD energetics that best approximate the observed events, and
3) employ the DNS results to assess the implied turbulence intensities and variability.

Overviews of PMC observations from the ground and from a stratospheric balloon over Antarctica are presented in Section 2. DNS methods and results employed for comparisons with these observations are described in Sections 3 and 4. Applications of the DNS results to the interpretation of PMC observations are discussed in Sections 5 and 6. These results are employed to estimate the magnitudes and variability of ε for the dynamics observed in the PMC fields in Section 7. A discussion of these results in relation to previous studies is provided in Section 8, and our summary and conclusions are presented in Section 9.

2. Observations of MLT Dynamics in PMCs

2.1. PMC Ground-Based Imaging in Norway

Ground-based PMC imaging was performed by G. Baumgarten from Trondheim, Norway (63.4°N) on 1 August 2009. A Canon 50D with a 135-mm lens provided continuous imaging at a cadence of ~0.5 s in a narrow field-of-view (FOV) of ~28x41 km (horizontal and range) at a central elevation angle of ~21° and a horizontal range of ~250 km yielding zonal and meridional resolution of ~10 and 20 m. A Canon 450D with a 24-mm lenses provided wide FOV imaging of the PMC layer over an area of ~600x600 km at a cadence of ~30 s.

2.2. Lidar Measurements of PMC in Norway

The Rayleigh lidar at the Arctic Lidar Observatory for Middle Atmosphere Research (ALOMAR) in northern Norway (69.3°N) supports multiple measurement modes (see, e.g., von Zahn et al., 2000; Baumgarten et al., 2012; Kaifler et al., 2013). For our purposes, it employed a lidar single-shot acquisition (LISA) capability to measure PMC backscatter and vertical displacements at range and time resolutions of 25 m and 0.033 s. The implications of these measurement will be discussed below.

2.3. PMC Observations from the Southern Hemisphere Stratosphere

PMC imaging was obtained serendipitously by star cameras for the E and B Experiment (EBEX), which measured the polarization of the cosmic microwave background from a stratospheric balloon over Antarctica from 29 December 2012 to 9 January 2013 (M15). Star camera field-of-views (FOVs) of 4.1x2.7° from an altitude of ~35 km at zenith angles of ~39 and 43° yielded ~4.4x3.9-km projected FOVs at the altitude of maximum PMC brightness, ~82 km, a range of ~62 km, and a central image separation of ~5.8 km. The narrow star camera FOVs yielded spatial resolution of ~2.2 m, thus resolving the inner scale of turbulence, $l_0=9.9(\nu^3/\epsilon)^{1/4}$~10 m, for ν~1 m^2s^{-1} and ϵ~1 m^2s^{-3} at 82 km (see comparisons with rocket measurements below), when apparent PMC advection was small. The close alignment of the two star camera FOVs, and the imaging cadence of ~450 ms, provided multiple cases in which the same dynamics in the same or closely-spaced regions were imaged 2 or more times. During the 11-day experiment, the star cameras collected ~40,000 images, of which ~50% provided usable images for purposes of assessing small-scale instability and turbulence dynamics.

3. DNS Models and Simulation Parameters

As noted above, we expect many types of instabilities to lead to turbulence in the MLT. Of these, GWs having vertical wavelengths λ_z~2 km or larger and relatively high intrinsic frequencies, $\omega_i >> f$, where f is the inertial frequency, readily lead to breaking via either 2D and/or 3D instabilities, depending on the environment and the relevant Reynolds number, defined as $Re=\lambda_z^2/\nu T_b$ with buoyancy period $T_b=2\pi/N_0$ (Fritts et al., 2009a, b, hereafter F09a, F09b),. At much smaller ω_i, e.g., within a factor of ~2-3 of f, the dominant instabilities at Richardson numbers $Ri=N^2/(dU/dz)^2=N^2h^2/U^2<1/4$ and $Ri<0$ are KHI (Lelong and Dunkerton, 1998a, b; Thorpe, 1999). GW distortions and intensification of local sheets of high stability and wind shear also lead to KHI that may be highly localized (e.g., Hecht et al., 2005, 2014; F13, F14b, F14c, F16). However, F14b found very weak turbulence to occur for Ri=0.2 and Re=2500, while flows for Ri=0.05 and Re=1000 become 3D but remain laminar. Thus, the latter are a very conservative threshold for turbulence generation and these yield $h=15(\nu/N)^{1/2}$. Taking ν~1 m^2s^{-1} and N~0.03 s^{-1} for a weakly stratified sheet (as opposed to a layer having N~0.01 s^{-1} or less), we obtain a threshold wavelength λ_{xT}~$4\pi h$~1.1 km below which KHI remain laminar. KHI at smaller Ri and larger Re have already been studied via DNS and high-resolution observations (e.g., F14b, F14c), and will not be considered here. Importantly, those studies suggested an often significantly larger effective turbulent viscosity, ν_{turb}, that could further decrease Re and λ_{xT}~ $\nu_{turb}^{1/2}$ by ~3 times or more for new instabilities. The other major instabilities occurring in observed flows and simulated MSD are intrusions (see M15 and F16). These do not appear to provide direct evidence of the spatial scales of the MSD, however they do distinguish MSD from more idealized flows. Given this, our focus here will be on modeling of GW breaking and MSD for comparisons with observations.

3.1. Equations

Our applications of DNS of GW breaking and MSD to MLT turbulence employ our previous results scaled to MLT events and turbulence intensities (e.g., F09a; F09b; F13; F16). These involve solutions of the 3D, Boussinesq, nonlinear Navier-Stokes equations, which are nondimensionalized with respect to a primary GW vertical wavelength λ_z, a uniform buoyancy period T_b, and the velocity scale $U_0=\lambda_z/T_b$. The resulting equations may be written as

$$\partial \boldsymbol{u}/\partial t+\boldsymbol{u}\bullet\nabla\boldsymbol{u}=-\nabla p+Ri\,\theta\mathbf{z}+Re^{-1}\nabla^2\boldsymbol{u} \qquad (1)$$

$$\partial\theta/\partial t+\boldsymbol{u}\bullet\nabla\theta=(Pr\,Re)^{-1}\nabla^2\theta \qquad (2)$$

$$\nabla\bullet\boldsymbol{u}=0 \qquad (3)$$

Here $\boldsymbol{u}=(u,v,w)$, p, and θ are the total velocity vector, pressure, and potential temperature, $N^2=(g/\theta_0)\mathrm{d}\theta_0/\mathrm{d}z=g\beta/\theta_0$, g, θ_0, and β are gravity, mean θ and its gradient, and $\mathbf{z}$ is a unit vector in the vertical. As previously, $Re=U_0\lambda_z/\nu=\lambda_z^2/\nu T_b$, $Ri=N^2\lambda_z^2/U^2,=4\pi^2$, and the Prandtl number, $Pr=\nu/\kappa=1$ (where κ is thermal diffusivity), is assumed for computational efficiency (e.g., F09a).

The linear inviscid dispersion relation arising from Eqs. (1-3) is given by

$$m^2=(k^2+l^2)(N^2/\omega_i^{\,2}-1) \qquad (4)$$

where k and l are the horizontal wavenumbers along, and normal to, the direction of GW propagation, m is the vertical wavenumber, $\omega_i=k_hc$ is the GW intrinsic frequency (assuming zero large-scale mean wind), $k_h^2=k^2+l^2$, c is the GW horizontal phase speed, and we assume mean wind shear and curvature to be negligible. The primary GW wavenumber vector for each DNS is $\boldsymbol{k}=(k,l,m)=(2\pi/\lambda_x,0,-2\pi/\lambda_z)$ in geographic coordinates. A tilted computational domain is employed for both GW breaking and MSD applications (see Fig. 1), yielding a primary GW wavenumber of $\boldsymbol{k'}=(k',l',m')=(0,0,-1)$, which allows a much more compact computational domain for $m/k>>1$.

Following Andreassen et al. (1998), we employ the negative eigenvalue (λ_2) of the tensor $\boldsymbol{L}=\boldsymbol{\Omega}^2+\boldsymbol{S}^2$, where $\boldsymbol{\Omega}$ and $\boldsymbol{S}$ are the rotation and strain tensors, to identify flow features having strong rotational character (Jeong and Hussain, 1995). Such features have large negative λ_2, whereas pure shearing motions yield $\lambda_2=0$. Thus λ_2 allows us to follow the transition from initial instability structures, through vortex interactions and instabilities, to fully developed turbulence and decay. We also compute the mechanical energy dissipation rate, defined as $\varepsilon=2Re^{-1}\langle S_{ij}\,S_{ij}\rangle$, to provide estimates of ε for these various dynamics for the observed MLT event scales.

3.2. GW Breaking Configuration

We employ previous DNS of GW breaking (F09a; F09b) for initial GW amplitudes $a=u'/c_i=0.9$ and 1.1 (for intrinsic phase speed $c_i=(c-U)$ and mean wind U along c), an intrinsic frequency $\omega_i=N/3.2$ ($T_{GW}=3.2T_b$), and $Re=\lambda_z^2/\nu T_b=10{,}000$. The computational domain has dimensions $(X',Y',Z')=(3.4,2.22,1)\lambda$, where $\lambda=2\pi/|\boldsymbol{k}|$ is the GW wavelength (see Fig. 1a). The two cases require comparable spectral resolution, with as many as $(N_x,N_y,N_z)=(2400,1600,800)$ Fourier modes employed at the times of strongest small-scale turbulence. The underlying dynamics are described in detail by F09a and F09b. Applications to instability forms and turbulence structures observed in PMCs are described in Section 4.

3.3. MSD Configuration

MSD employed here are those described by F16 at $Re=100{,}000$, which achieve $Re_b\sim20$-30 during the strongest turbulence, and scaled to the MLT. As in F16, initial conditions include a convectively stable GW and a stable small-scale shear flow. The GW has an amplitude $a=0.5$, $\omega_i=N/10$ ($T_{GW}=10T_b$), wavenumber $(k',l',m')=(0,0,-1)$, and exhibits a minimum $Ri\sim4$ where $d\theta'/dz\sim0$ and $du'/dz\sim N/2$. The initial mean motion is given by a sinusoidal streamwise velocity having 5 cycles across the vertical projection of the GW λ having $(dU/dz)_{max}=2N$ such that the minimum mean shear is $Ri=¼$. The streamwise and spanwise domain extents are $X'=Z'/(5\tan\phi)=1.999Z'$ and $Y'=0.5\lambda_z=0.4975Z'$ (see Fig. 1b). The highest model resolution used for this DNS is (4320,1080,2160) Fourier modes. These MSD, and their implications for instability and turbulence structures observed in PMCs, are described in Sections 4 and 5.

3.4. Simulation of PMC images

The instability dynamics examined here occur on timescales of only a few minutes. Over such short intervals, PMC brightness can be approximated as a passive tracer (G. Thomas, PC, 2016: Chandran et al., 2016). Hence, we parameterize PMC brightness as a function of the initial θ_0, which is monotonically increasing and nearly conserved following the air motion, as

$$B(z) = B_0 \exp[-(z - z_{PMC})^2/2\sigma_z^2] = B_0 \exp[-(\theta_0 - \theta_{PMC})^2/2\sigma_\theta^2] \quad (5)$$

where z_{PMC} and θ_{PMC} are PMC altitude and θ_0 at the peak of PMC brightness and $\sigma_z = z_{FWHM}/2(2\ln2)^{1/2}$ corresponds to an PMC layer having a typical full width-half maximum

(FWHM) brightness of z_{FWHM}. Examples of Rayleigh lidar observations at ALOMAR described above are shown for reference in Fig. 2. These reveal that the PMC brightness layer can have z_{FWHM} as small as ~50-100 m, and perhaps less, accompanying strong layering in the presence of energetic small-scale GW and instability dynamics. Additional evidence for such thin layers accompany observed and DNS MSD flows that yield $d\theta/dz$ and N^2 maxima up to 10 times mean values or larger and high *Re* (F16, and references therein). This is a particularly useful feature of PMC layers because it provides a potential to observe structures occurring at very small scales.

4. DNS of Idealized GW Breaking and MSD

4.1. DNS of GW breaking, instabilities, and turbulence

Floquet theory employed by F09a suggested initial GW instabilities comprising streamwise-aligned (streamwise vorticity, spanwise wavenumber) counter-rotating rolls. The parallel DNS show these to be approximately horizontal initially, and to evolve to finite-amplitude and induce intensifying vortex sheets above (below) having negative (positive) streamwise vorticity (Andreassen et al., 1998). These dynamics are illustrated in Figs. 3 and 4 with volumetric views of λ_2 at $1T_b$ intervals beginning before strong breaking for GW amplitudes a=0.9 and 1.1 and other parameters specified above. Note that we have displayed these fields with GW propagation upward and to the right in order to have the same orientation as in the ground-based PMC imaging discussed below.

Where these vortices dip below the coldest phase of the GW (above the maxima of u' and w'), they interact with the spanwise vortex sheets above the most unstable (smallest N^2) phase of the GW. The downward motions induce stretching and intensification of the opposite spanwise vortex sheets below, and these structures link to form a succession of vortex rings along the GW phase that expand in time and advect upward at the maxima of u' and w' along c, though at a velocity smaller than c (Figs. 3 and 4; panels a, b, e, and f). The resulting vortex rings yield plunging motions downward and in the direction of GW propagation (Figs. 3 and 4; panels f and g). They also cause coherent linkages between adjacent GW fronts that act to organize the transitional instability structures that cannot be seen in the λ_2 volumetric views in Figs. 3 and 4.

Thereafter, strong interactions among adjacent vortices induce "twist-wave" perturbations of the various vortex structures that cause their fragmentation and rapid collapse to smaller scales comprising the turbulence cascade (Figs. 3 and 4; panels b-d and f-h; F09b; Andreassen et al., 1998; Fritts et al., 1998). The evolutions from coherent vortex rings to strong turbulence span ~$1T_b$ or less, or a few minutes for a typical mean N, with a more rapid evolution at a larger amplitude and/or higher ω_i (new paper in preparation).

4.2. DNS of MSD, instabilities, and turbulence

As noted above, instabilities exhibit many forms in MSD flows throughout their evolutions. These arise as a result of interactions among the larger-scale mean and GW motions that largely account for the S&L structures and the instability and turbulence dynamics induced within them. Examples of the S&L structures and instabilities occurring at several stages of an MSD DNS described by F16 are shown in the $N^2(x,z)$ and $\log_{10}\varepsilon(x,z)$ fields at left and right in Fig. 5. Color scales in both cases are from weak (blue) to strong (red), N^2 varies by more than a decade, and ε varies by more than 4 decades at each time. Strong GW breaking and large-scale KHI arise at early stages following S&L formation when large GW amplitudes and shears provide significant energy sources for instabilities and turbulence (e.g., Fig. 5, panels a-d and g-j). At later stages, instabilities are weaker and more intermittent, turbulence is weaker and more confined vertically, and intrusions (e.g., Fig. 5, panels e, f, k, and l) play a competitive role with weaker GW breaking events.

Finally, we note that both the idealized GW breaking and MSD dynamics are described in a Boussinesq DNS having specified initial conditions. As such, they are "spin-down" DNS without continuous energy inputs by GWs propagating from below. This does not limit the ability to compare instability dynamics and/or turbulence intensities with atmospheric observations at low or high altitudes (e.g., F13, F14b, F16) at sufficiently high Re. But the earlier times in each DNS having more energetic GWs, instabilities, and turbulence are more representative of atmospheric conditions in which there are significant GW fluxes of energy to higher altitudes. In contrast, the later times in each DNS more closely approximate times where

GW vertical energy fluxes are relatively weak. The DNS of idealized GW breaking and MSD described here are employed below to interpret and quantify instability dynamics and turbulence intensities observed in PMCs from the ground and a stratospheric balloon. The former provides continuous viewing of dynamics that may span multiple T_b; the latter does not track the evolutions of specific dynamics, but does provide valuable insights into small-scale instability and turbulence dynamics that are impossible to obtain at any other altitude in the atmosphere.

5. GW Breaking Dynamics Observed in Ground-Based PMC Imaging

We first examine an apparent GW breaking event observed over northern Norway on 1 August 2009. These dynamics occurred following an extensive display of KHI beginning ~22:30 UT, having constant phases aligned roughly northwest to southeast (NW-SE), advecting towards the southwest (~40^{o} W of S) at ~70 ms^{-1}, and exhibiting very slow evolutions in time (e.g., individual KH billow events spanning ~10 min or longer). This display includes the KHI *Ri*~0.20 event described in detail by Baumgarten and Fritts (2014) and F14b. Throughout, the KHI structures exhibited significant modulations in phase and amplitude (see Fig. 6a), suggesting a complex shear environment likely reflecting spatial variations accompanying small-scale GWs.

Measurements of large-scale winds at these altitudes were available only by the meteor radar at ALOMAR, ~450 km N of the observations from 22 to 24 UT. These had 2-km and 1-hr resolution, but appeared to be consistent with observed PMC advection at ~82 km and our expectation of mean winds towards the SW decreasing with altitude during summer.

Beginning at ~23:10, larger-scale PMC brightness variations became apparent that suggest GW modulations of the wind and temperature fields and the PMC layer on larger spatial scales. Extended KHI structures persisted in the presence of the larger-scale GWs at several locations beyond ~23:20 (see Fig. 6). Despite more complex KHI structures at small spatial scales, their evolution timescales did not change appreciably. However, the wind shears enabling KHI apparently diminished with time, and evidence of KHI disappeared thereafter (e.g., see the outer edges of the PMC images at 23:30 and thereafter in Fig. 6).

The GW field contributing to the changing instability environment had several apparent components: 1) one having a horizontal wavelength λ~70 km and propagating slowly towards the southeast (SE) throughout, 2) a second having λ~30 km and propagating more rapidly towards the north-northeast (NNE) from 23:30-50, and 3) a third localized GW having λ~50 km, a large amplitude from ~23:30-50, and propagating towards the south-southeast (SSE). These GW phases and propagation directions are shown with the white, red, and pink lines and arrows in Fig. 6b-d, respectively. Of these, the large-amplitude, smaller-scale GW propagating towards the SSE appears to have had the largest influences on instability forms and alignments in the region highlighted by the yellow circles in Fig. 6. Hence, we will assume this GW was the major cause of the instabilities seen to occur after 23:30 in Fig. 6, though the others likely also contributed to the local shear and stability fields. Shown with a green trapezoid in Fig. 6c is the region in which we will focus our discussion of the instability dynamics during this event.

The dominant GW initiated a series of bright bands aligned nearly along its direction of propagation at two phases at 23:30 and 23:40 (see the features within the yellow circles in Fig. 6b and 6c). These features are very similar to those previously associated with GW breaking seen in PMC (Fritts et al., 1993), and seen prior to the formation of vortex rings in the DNS shown in Figs. 3 and 4. In this case, however, the two primary GW phases were neither linear nor parallel due to the influences of other GWs also present. Initial streamwise-aligned features were more distinct at 23:30 prior to the occurrence of instabilities between these phases. Changing GW superpositions and induced instabilities in this region thereafter extended beyond 24:00.

By 23:40, small-scale instabilities having 3D character appeared in the lee of the leading GW phase at lower right (to the NW). These initial dynamics are shown from 23:42-45 UT at 1-min intervals in Fig. 7a-d. The volume viewed is shown with the green trapezoid in Fig. 6c and the viewing angle for these images is from ahead and to the right of the primary GW propagation direction, and below the horizontal plane of the PMC by ~21^{o}. The images in Fig. 7a and 7d are also shown mapped and viewed from above to show their true spatial scales in Fig 7e and 7f. As in the DNS, the initial bands assigned the scales of the subsequent 3D instability features seen in their lee. Additionally, the time scales of the instability dynamics changed dramatically between 23:30 and 23:40. Whereas KHI observed prior to ~23:40 evolved over several T_b, the apparent GW breaking dynamics shown in Fig. 7 evolved significantly over 3 min (~0.6 T_b).

The images at top reveal complex structures that we identify as vortex rings that appear to be overlapping because of the shallow imaging slant view. In reality, the vortices are likely displaced horizontally rather than vertically within the GW field, as they occur at only one phase of the DNS of GW breaking seen in Figs. 3 and 4. Their alignments appear to have been at successive positions along the plane of GW propagation (lower left to upper right in Fig. 7a-d), with apparently overlapping vortex rings staggered at adjacent horizontal locations normal to the plane of GW propagation, as seen in the DNS, especially Fig. 3. Their diameters at these times were as large as ~8-10 km, and likely ~20-50% larger than when they first formed at smaller amplitudes, based on the expansions seen in the DNS results. Our DNS reveal that vortex ring spacing along the plane of GW propagation, and between vortex rings occurring on adjacent vortex sheets, varies with GW amplitude and intrinsic frequency, and likely with the background wind shear and orientation, however. In particular, new DNS reveal that vortex ring spacings and evolution timescales decrease with increasing ω_i (L. Wang, pers. comm., 2016).

The three initial vortex rings at the more southward locations (upper and lower portions of the yellow ovals in Fig. 7a and 7e, respectively) exhibit bright trailing vortices extending generally upward and to the west from their interiors (as in Figs. 3b and 4b) due to the viewing geometry. Especially significant in this sequence is the rapid decay of the coherent vortex rings over its 3-min (~0.6 T_b) duration that is consistent with their decay time scale seen in the DNS results in Figs. 3 and 4. This is dramatically faster than the evolutions of the earlier KHI at the PMC altitude and is a clear distinction between KHI and GW breaking dynamics. Additional, but less distinct, features are also seen to the west and north (left and below in Fig. 7a-d) of those highlighted, and they likewise decay over the same interval.

We explore these comparisons further using Eq. (5) to compute PMC brightness fields for the GW breaking events shown in Figs. 3 and 4 at four times with a PMC layer thickness of

z_{FWHM}=0.1 λ_z. The results for a=0.9 from 21-22 T_b and a=1.1 from 10.2-11.2 T_b at 0.33 T_b intervals are shown viewed from below at left and right in Fig. 8, respectively. In each case, the PMC layer was placed to coincide with the vortex rings in the most unstable phase of the GW. Both cases exhibit trailing vortices, as seen in the PMC images, and a rapid evolution from coherent vortex rings to turbulent motions over ~1 T_b. That with a=0.9 more clearly illustrates vortex ring expansion; that with a=1.1 exhibits a more rapid vortex ring breakdown to turbulence and a smaller vortex ring spacing (given periodic boundaries, Fig. 11d).

The subsequent evolution of this region shown from 23:47-50 UT in Fig. 9a-d reveals the further breakdown of the vortex rings discussed above (see yellow ovals). These images also suggest the development of new vortex rings at even larger scales (see the brightening curved features at the right edges of Fig. 8e and 8f), but these are seen primarily in the wide FOV, as they advect out of the narrow FOV to the SW over the next ~5 min.

6. GW Breaking Dynamics and MSD Observed in Stratospheric PMC Imaging

Miller et al. (2015) reported an initial exploration of serendipitous PMC imaging from a stratospheric balloon in the interpretation of dynamics near 82 km. Here, we perform additional comparisons of stratospheric imaging of PMCs and DNS modeling to quantify the character, scales, and energetics of key instability dynamics arising due to GW breaking and MSD at PMC altitudes. This process enables estimates of the contributions of these dynamics to the energy dissipation rate ε in the MLT presented in Section 7 below.

Many PMC images obtained by the EBEX stratospheric balloon experiment include features that appear to be evidence of either relatively monochromatic GW breaking, smaller-scale KHI, or more complex MSD events (Miller et al., 2015). These can often be identified by PMC brightness variations arising due to advection and deformation of the PMC layer by larger- and smaller-scale GWs, their various instability forms, and turbulence structures. The unique aspect of these observations is the extremely high spatial resolution that can be achieved in cases where the PMC layer is very thin accompanying the underlying dynamics, e.g., resolving features having spatial scales as small as ~10-20 m.

6.1. GW breaking dynamics observed in stratospheric PMC imaging

Two examples that appear to be at relatively early stages in the evolution of a breaking GW are shown in Fig. 10a and 10b. These do not correspond to the same event, as EBEX imaging only occasionally, and accidentally, acquired images of the same PMC field spaced by 10's of seconds or more. Nevertheless, the two images appear to capture features that we recognize as slightly different stages of breaking GW. That in Fig. 10a closely resembles a simulated PMC (Fig. 10c) suggesting the overturning "front" for the GW breaking case with a=1.1 and z_{FWHM}=100 m at a time just after that in Fig. 4b. That in Fig. 10b suggests a strange diagonal pattern that likewise resembles a simulated PMC (Fig. 10d) for the GW breaking case with a=0.9 and z_{FWHM}=100 m at a time near that in Fig. 3b. These images indicate that there are occasions when the larger-scale MLT dynamics (i.e., vertical scales larger than the S&L scales in MSD) are characterized locally by approximately monochromatic GW breaking rather than less energetic MSD. The apparent overturning front reveals approximately streamwise vortices at the initial stages of instability that may allow an estimate of the depth of the layer that is unstable, based on the spanwise (along the front) spacing of the major vortex features. Comparing the characteristic spacing with the DNS suggests a vertical wavelength of λ_z~2-4 km, but provides little guidance on λ_h or ω_i. The diagonal patterns in Fig. 10b and 10d suggest a λ_h>5 km, given that the true PMC image does not capture the full streamwise GW phase structure.

More quantitative assessments are possible in cases where specific instability dynamics directly related to intrinsic GW parameters are observed. The clearest examples of such at larger spatial scales identified to date appear to be vortex rings, as simulated in the GW breaking DNS shown in Figs. 3 and 4, and as seen in initial EBEX PMC imaging (Miller et al., 2015). Images of apparent vortex rings in three different events are shown in Fig. 11a-c. That in Fig. 11a shows the full image having a horizontal FOV of 4.4x3.9 km and reveals a well-developed vortex ring diameter of ~4 km and a spacing between rings of ~4 km. The diameter is indicative of a GW λ_z~8-10 km, and the close spacing is suggestive of ω_i~N/3 or greater. Additionally, the apparent bright trailing vortices extending to the lower right of the vortex rings suggest vortex ring selfadvection and GW propagation towards the upper left. A simulated PMC from the DNS shown in Fig. 11d for a GW propagating upward (as seen from below) is shown for comparison in Fig. 11d. This captures the darker vortex rings, their successive displacements, and an indication of brighter trailing vortex features, suggesting agreement of the underlying dynamics.

Fig. 11b shows another apparent vortex ring that was propagating largely away from the viewing platform (downward in the PMC image), based on the orientation of the bright trailing vortices. This vortex ring had a diameter of ~1.5-2 km and appeared to be undergoing breakdown (as seen in Figs. 3c and 4c), or to have occurred in an already turbulent region. It had no other vortex rings in close proximity, suggesting an ω_i comparable to, or lower than, shown in Figs. 3 and 4, based on DNS observations of closer vortex ring spacing at ω_i~N/2 to N/1.4.

Fig. 11c shows a PMC image that reveals an apparent succession of vortex rings that had similar character, were apparently linked by trailing vortices, and were self-advecting towards the right, suggesting GW propagation in this direction. These features are strikingly similar to a simulated PMC using the DNS for a=1.1 at ~10.5 T_b, a short time following the image in Fig. 4b. The diameters of these structures are up to ~1 km and they appear to be closely spaced along the GW propagation direction, suggesting a GW λ_z~2 km and ω_i~N/3 or larger in this case.

6.2. MSD observed in stratospheric PMC imaging

EBEX stratospheric PMC imaging has also yielded multiple examples that confirm DNS predictions of various MSD flows, several of which are described below. Fig. 12a shows what appear to have been cusp-like structures having longitudinal scales of up to ~1 km, lateral scales of ~100-300 m, some organization of these features in lateral rows, and apparent strong shearing of the lower edges towards the lower left (along the arrow).

The simulated PMC image in Fig. 12b was obtained using the method described in Section 3.4 with z_{FWHM}=200 m at the bottom edge of the region of local GW breaking having large ε shown in the black oval in Fig. 5h. Inspection of the corresponding N^2 field in Fig. 5b reveals this to be a sheet having elevated stability, and the corresponding velocity field (not shown) confirms a significant wind shear with increasing winds at lower altitudes along the arrow. As in Fig. 12a, cusp-like features seen in Fig. 12b exhibit apparent shearing consistent with the wind direction below, some lateral alignments, and lateral scales of ~5-10% of the MSD domain width (~λ_z/2). Finally, we note that the cusp-like features in Fig. 12 have many similarities to the vortex rings identified at larger spatial scales, including ring-like highlights and streamwise vortices extending from their centers a multiple sites in the observed and simulated fields. Thus, they could be manifestations of small-scale GW breaking in a more chaotic environment.

Equating the cusp scales between the EBEX and MSD simulated PMC images suggests an MSD overall depth of ~6 km. This scale is less important in this case than the S&L spatial scales that constrain this event. This depth is likely ~1 km in this region of the MSD flow, based on the DNS shown in Fig. 5. Hence, we expect the MSD DNS to provide a reasonable approximation of the associated ε for these specific dynamics in the discussion below.

Other instabilities that are seen in a number of stratospheric PMC images are intrusions. Two examples are shown in Fig. 13a and 13b. Their apparent directions of motion are shown with arrows and the image widths are ~3 and 4.4 km, respectively. These observations confirm the occurrence and importance of these dynamics predicted by the MSD DNS, at least in cases where other dynamics that lead to stronger turbulence are not present (F13, F16). An intrusion occurring in the MSD DNS at late times is shown evolving from a laminar to a turbulent flow in Fig. 5k and 5l. Simulated PMC responses assuming a PMC z_{FWHM}=100 and 300 m in the region within the black oval in Fig. 5l are shown in Fig. 13c and 13d to illustrate the sensitivity of the PMC response to the PMC layer depth. These reveal that thinner layers provide greater sensitivity to smaller-scale dynamics, as argued above. Unlike GW breaking, there is no current way to evaluate ε for intrusions without a means of assessing their scales. This may change in cases where their depths, relative motions, and/or turbulence spectra can be directly assessed.

7. Energy Dissipation Rates in the MLT

The discussion above identified four events observed in PMC imaging from the ground and stratosphere that compare reasonably with DNS of GW breaking for idealized and MSD flows and enable some quantification of GW parameters. These allow DNS results to be scaled to the observed dynamics that enable estimates of ε for the observed events at PMC altitudes. The cases for which this can be done with some confidence include the following:

Case 1: GW breaking over Norway (Fig. 7) exhibiting vortex rings having initial diameters of ~7 km or larger suggesting a GW having $a>1$, $\lambda_z\sim15$ km or larger, and $\omega_i>N/3$,

Case 2: vortex rings (Fig. 11a) having diameters of ~4 km suggesting GW breaking for $a\sim1$, $\lambda_z\sim8$-10 km, and $\omega_i>N/3$,

Case 3: vortex rings (Fig. 11c) having maximum diameters of ~1 km suggesting GW breaking for $a\sim1$, $\lambda_z\sim2$ km, and $\omega_i>N/3$, and

Case 4: cusp patterns in a MSD S&L flow (Fig. 12) suggesting GW breaking over ~1 km and an MSD domain depth of ~6 km.

Estimates of MLT turbulence intensities for these events require scaling the nondimensional DNS to the observed dynamics and inferred spatial scales. For both idealized GW breaking and MSD, the scaling factor is $S=\lambda_z^2/T_b^3$. S will vary by ~2 decades because of the large range of $\lambda_z\sim2$-15+ km inferred in our discussions of the events above. S will also vary with N, which is determined by temperature fields on larger scales than the GW breaking event, i.e., mean, tidal, planetary wave, and larger-scale GWs, that can be measured by ground-based and *in-situ* instruments. Where these are unknown, uncertainties could be as large as ~2 in the large-scale N based on *in-situ* measurements to date. We have no direct measurements of N for any of the PMC events discussed here. However, the mean PMC environment at ~82 km over ALOMAR has $T\sim150$ K, $N\sim0.023$ s^{-1}, and $T_b\sim270$ s (Rapp et al., 2004). Below, we examine the implications of each of the above cases for MLT instability event scales and turbulence intensities, assuming these values for our analyses. Event parameters are listed in Table 1.

7.1. Case 1: GW breaking with $\lambda_z\sim15+$ km

The GW breaking event observed over Norway revealed large-scale vortex rings implying a GW having $a>1$, $\lambda_z\sim15$ km or larger, and $\omega_i>N/3$. Together, these parameters imply that the GW breaking DNS for a=1.1 shown in Fig. 4 represents a conservative estimate of the instability and turbulence intensities for this case, perhaps by a significant factor.

Horizontal distributions of nondimensional ε at the times of largest mean $<\varepsilon>$ (where brackets denote a domain average) for a=0.9 and 1.1 (i.e., Figs. 3d, 3h, 4d, and 4h) viewed from below and the side (with GW propagation up and to the right) are shown in Fig. 14a, 14b, 14e, and 14f. The same views of the thermal energy dissipation rate in the energy equation, $Ri\chi$ (F16), are shown in Fig. 14c, 14d, 14g, and 14h. These reveal that despite strong vortex interactions, turbulence generation, and mixing along the most unstable phase of the GW spanning several T_b, ε and $Ri\chi$ are highly variable spatially. These fields in Fig. 14 are reasonably correlated at larger spatial scales, but their maxima often are not. In particular, there are many cases in which ε and $Ri\chi$ maxima occur in close proximity, but are displaced horizontally and/or vertically where strong mixing has driven the strong thermal gradients to the edges of the mixing regions.

Probability distribution functions (PDFs) of $\log_{10}\varepsilon$ for a=0.9 at 21, 22, 24, 30, and 40 T_b are shown in Fig. 15a. Those for a=1.1 at 9.2, 10.2, 12.2, 20, and 30 T_b are shown in Fig. 15b. The two earliest times in each case are during the onset of turbulence at larger spatial scales. As the initial vortex rings evolve, the PDFs acquire approximately log-normal distributions, and these persist to very late times. The strongest turbulence in each case occurs ~2 T_b after vortex ring formation, and $<\varepsilon>$ and ε_{high} (above which the highest 1% of ε occur) are shown with vertical lines in Fig. 15a and 15b. These are ~0.7-1.1 decades larger than at the times of initial coherent vortex rings for a=0.9 and 1.1, respectively. Hence, we expect maximum turbulence to occur ~8-10 min after the appearance of coherent vortex rings (and large-scale u', w', and T' for typical summer mesopause stability profiles). PDFs of $Ri\chi$ (not shown) exhibit similar behavior following the onset of instabilities and turbulence (e.g., F09b). Because of the broad, approximately log-normal distributions of ε and χ accompanying turbulence (they span ~4 decades at the times of strongest turbulence), only ~15-20% of the values are above their domain means. Even for the vertical and spanwise means shown in Fig. 14 (which have narrower distributions spanning only ~2 decades, see the color bars in Fig 14; also see the local PDFs in Fig. 8 of FW13), the largest values are strongly localized at the sites of the previous vortex rings.

To explore the relations between the maxima of ε and $Ri\chi$ more directly, we average these quantities over 64 adjacent points to provide high confidence in these values, yielding values at ~10^8 locations. As above, this reduces the range of values, but these still span >3 decades. Scatter plots of these values for the larger 0.1-0.01% (black dots) and 0.01-0.001% (green triangles), and the largest 0.001% (red squares) of ε and $Ri\chi$ are shown in Fig. 16a and 16b, respectively.

Examining first Fig. 16a, we see that the largest ε are clustered at quite small $Ri\chi$, but that there are also multiple sites where $Ri\chi$ is comparable or larger. The former likely arise where strong mixing of the thermal gradients has already occurred, the latter likely are from regions within the strongly stratified and sheared sheets within which turbulence events first arise and strong thermal and velocity gradients are still entwined. Distributions for the largest $Ri\chi$ exhibit different behavior. And there is almost no overlap between the largest 0.001% of ε and $Ri\chi$, at most 4 locations in ~10^8. The largest $Ri\chi$ typically accompany ε values between ~1 and 10% of the maximum, thus apparently do not have much smaller associated ε. This is because small-scale velocity gradients (and significant ε) are required to maintain strong thermal gradients.

Turning to implications of these dynamics for turbulence intensities, we dimensionalize the PDFs for a=0.9 and 1.1 by $S=\lambda_z^2/T_b^3$=11 Wkg^{-1} (or m^{2}s^{-3}), yielding maxima of $<\varepsilon>$~0.22 and 0.55 Wkg^{-1} and ε_{high}~2.4 and 6 Wkg^{-1} for these cases, given the separations between their locations shown with vertical lines in Fig. 15a and 15b. The mean values $<\varepsilon>$ are comparable to, or larger than, the largest estimates by in-situ probes at PMC altitudes of ~0.3 Wkg^{-1} (e.g., Strelnikov et al., 2009). The implied ε_{high} are much larger than have been observed at these altitudes, especially as the inferred GW parameters suggest that the likely $<\varepsilon>$ and ε_{high} are larger than those for a=1.1.

There are several explanations that appear plausible. Very large $<\varepsilon>$ and ε_{high} likely accompany very strong events that are infrequent and most often highly localized spatially and temporally; see, e.g., the strong spatial localization implied by the broader PMC fields shown in Fig. 6 and the transience (i.e., a duration of ~1-2 T_b) of strong maxima implied by Figs. 14b, 14f, 15a, and 15b. Hence, the likelihood that any single rocket measurement would observe such an event at the location and time of maximum $\langle\varepsilon\rangle$ is very small, perhaps less than 0.1%. This fraction would increase significantly, of course, where ground-based measurements were able to provide real-time identification of specific events and expected times of maximum turbulence. The likelihood of observing $\langle\varepsilon\rangle$ and/or ε_{high} even sampling such an event is also small because of the limited portions of the GW and turbulence field that have large $\langle\varepsilon\rangle$ and/or ε_{high} along a single near-vertical rocket trajectory implied by the horizontal ε fields in Fig. 14a and 14b. ***Indeed, sampling a turbulence field having high intermittency would require multiple vertical profiles to develop confidence that a representative mean value was likely to be obtained.***

Another reason that sampling $\langle\varepsilon\rangle$ and/or ε_{high} using current in-situ instruments is challenging is that they measure temperature rather than velocity fluctuations, hence estimate the turbulence spectral shape where $Ri\chi$ may be small and thus have a low spectral amplitude, despite large ε (see Fig. 16a). Finally, smaller measured than predicted ε_{high} may arise because in-situ measurements typically average over ~30-100 m along the rocket trajectory, whereas ε_{high} occur accompanying the strongest small-scale vortices (and largest velocity shears) near the turbulence inner scale, $l_0=9.9(\nu^3/\varepsilon)^{1/4}$~10 m or less (Lübken, 1997), accompanying the strongest events. Several of these influences can be evaluated by employing current in-situ measurement methods to sample our various DNS data, and we expect to perform such studies in the future.

7.2. Case 2: GW breaking with λ_z~8-10 km

The vortex rings shown in Fig. 11a have diameters of ~4 km and appear to have been observed prior to further instabilities (and ring expansion), implying GW breaking for a~1, λ_z~8-10 km, and ω_i~N/3. These parameters yield S~3-5 Wkg^{-1}, hence maximum $\langle\varepsilon\rangle$~0.06-0.1 and 0.15-0.25 Wkg^{-1} and maximum ε_{high}~0.7-1.1 and 1.6-2.6 Wkg^{-1} for the two cases shown in Figs. 3 and 4. These $\langle\varepsilon\rangle$ values are comparable to the larger values measured at the PMC altitude, i.e., $\langle\varepsilon\rangle$~0.1-0.3 Wkg^{-1} (e.g., Rapp et al., 2004; Strelnikov et al., 2009). These magnitudes suggest that such GW and instability scales may be somewhat more representative of those occurring more frequently at ~82 km.

7.3. Case 3: GW breaking with λ_z~2 km

The smaller vortex rings shown in Fig. 11c having maximum diameters of ~1 km imply GW breaking for a~1, λ_z~2 km, and ω_i>N/3, hence S~0.2 Wkg^{-1} or somewhat larger. These imply much weaker turbulence than suggested by the larger-scale vortex rings in Cases 1 and 2. Scaling in this case implies $\langle\varepsilon\rangle$~0.004 and 0.01 Wkg^{-1} and ε_{high}~0.04 and 0.1 Wkg^{-1} for a=0.9 and 1.1, with larger values if ω_i exceeds N/3 by a significant amount. These and smaller turbulence magnitudes should be expected for GW breaking events at quite small horizontal and vertical scales, such as might be implied by ~2-km vertical scales in lidar or in-situ $T'(z)$ profiles obtained with very little temporal averaging. Similar λ_z, but λ_h~10-30 km or larger, imply smaller $\langle\varepsilon\rangle$ and ε_{high} because of the smaller GW vertical group velocities of such motions.

7.4. Case 4: MSD with λ_z~6 km

The cusp patterns seen in Fig. 12a suggest GW breaking similar to that in a shallow layer of the MSD DNS shown in Fig. 5h assuming a domain depth of 6 km. PDFs of ε for this event are shown at 5, 10, 12, 22, and 32 T_b in Fig. 15c. For reference, time series of domain mean $[\varepsilon]$ are compared for the two GW breaking events and the MSD event described above in Fig. 15d. That for the MSD DNS is shown at 5x amplitude for comparison with the GW breaking DNS.

From the ε field shown in Fig. 5h, we see that the cusp-like features occur in a region that spans nearly the full range of ε in the full domain at the time of the cusp-like event. The inferred domain depth implies S~2 Wkg^{-1}, thus a maximum $\langle\varepsilon\rangle$~0.016 Wkg^{-1} at the time of the cusp occurrence, and ε_{high}~0.25 Wkg^{-1}.

8. Discussion

Our study has focused on identification of GW instability dynamics observed in PMC imaging, their spatial and/or temporal scales, and the turbulence intensities, $\langle\varepsilon\rangle$ and ε_{high}, anticipated via comparisons with high-resolution DNS of these dynamics. To achieve results with the highest confidence, we have focused on dynamics that were well defined in our various

PMC imaging, thus on events that exhibited the largest instability scales that could be identified. Because turbulence intensities vary as λ_z^2 for any event, our studies likely emphasized the stronger turbulence sources during these observations due to their more easily identified and quantified dynamics. Hence, the $<\varepsilon>$ and ε_{high} accompanying the most energetic phases of these events are surely significantly larger than mean values at these altitudes.

As an example, our range of estimates of $<\varepsilon>$~0.06-0.55 Wkg^{-1} at the most intense phases of the stronger events analyzed in detail mostly exceed the values observed in a PMC environment at ~82 km of ~0.001-0.3 Wkg^{-1} inferred in previous radar and in-situ assessments by up to ~20 times (e.g., Lübken, 1997; Lübken et al., 2002; Rapp et al., 2004; Engler et al., 2005; Latteck et al., 2005; Strelnikov et al., 2009; Szewczyk et al., 2013) and elsewhere at the same altitudes (e.g., Hocking, 1988). This is especially true given that we regard $<\varepsilon>$ and ε_{high} estimated using the GW breaking DNS for a=1.1, λ_z~15 km, and $\omega_i=N/3.2$ to be quite conservative for Case 1 with estimated GW parameters of $a>1$, λ_z~15 km or larger, and $\omega_i>N/3$. The estimate of ε_{high}~6 Wkg^{-1} for this case far exceeds all estimates at ~82 km and is comparable to the largest magnitudes (~1-10 Wkg^{-1}) reported near the mesopause in the papers cited above. The largest ε in Fig. 15 are another ~3 times higher.

Possibly more interesting, but to which PMC estimates can contribute only peripherally, are the larger and more continuous estimates of $<\varepsilon>$ as atmospheric stability increases approaching and above the polar summer mesopause. In-situ measurements at these altitudes have revealed relatively continuous turbulence intensities increasing from PMC altitudes to $<\varepsilon>$~0.03-1 Wkg^{-1} above ~85 km, with peak values as high as $<\varepsilon>$~2-10 Wkg^{-1} in each profile, and often occurring just above the mesopause (Rapp et al., 2004; Szewczyk et al., 2013). These measurements suggest that strong turbulence near the mesopause is apparently not intermittent, but more nearly continuous in space and time, despite the potential for under-estimates of true $<\varepsilon>$ magnitudes noted above.

Several aspects of MLT GW dynamics contribute to sustained, strong turbulence near and above the polar summer mesopause. There is a ubiquitous spectrum of GWs having various (and evolving) intrinsic parameters (a, λ_z, λ_h, ω_i, direction of propagation) that account for continuous fluxes of energy and momentum into the polar summer MLT from sources primarily at lower altitudes (e.g., Balsley and Garello, 1985; FV93; FA03). There are also environmental influences that cause GWs to increase in relative amplitude and lead to instabilities and turbulence throughout the atmosphere. These include the following:

1) continuous increases in GW amplitudes with increasing altitude due to decreasing density,
2) successive instability cycles at similar altitudes for GWs having large ω_i and λ_z due to only partial GW attenuation accompanying breaking (F09a, F09b),
3) successive instabilities at higher altitudes for large GWs with ω_i and λ_z due to only partial GW amplitude reductions accompanying breaking at lower altitudes,
4) wind shears due to mean, tidal, planetary wave, and larger-scale GWs that can induce decreasing λ_z and increasing a for GWs experiencing decreasing ω_i,
5) increasing N^2 that drives decreasing λ_z, increasing $u'/w' \sim \lambda_h/\lambda_z$ and a, hence increasing GW instabilities (VanZandt and Fritts, 1989, hereafter VF89; FV93), and
6) nearly continuous interactions among GWs that drive MSD instabilities in S&L flows.

The consequences of these dynamics are that GWs are always present in the MLT. To our knowledge, there are no PMC (or airglow) movies or images that do not reveal GW activity at larger and/or smaller spatial scales. The large majority of these also exhibit instability and/or turbulence dynamics, but these are often localized within the GW field and their detection depends on their amplitudes and the spatial resolution of the imager. Large-scale instabilities (horizontal scales up to 10 km or larger) that are easily detected can occupy from a few % to a majority of a large FOV. However, strong, local instabilities that evolve rapidly are often closely associated with the largest-amplitude (brightest) GWs having λ_h ~30-60 km or smaller. Strong turbulence likely accompanies the stronger instabilities, whereas weaker turbulence is long-lasting and thus assured and likely widespread, but very difficult to observe.

The various effects noted above are accounted for statistically in a spectral model of the evolution and dissipation of GWs with altitude (and varying N^2) that is constrained by observations and theory. The model initially addressed only increases in N^2 (VF89), but was later generalized to include realistic altitude variations throughout the atmosphere (FV93). This theory yields an estimate of $<\varepsilon>\sim 0.28$ Wkg^{-1} near the mesopause without the enhanced contribution due increasing N (FV93); the enhanced $<\varepsilon>$ (and $\varepsilon>\varepsilon_{high}$) may be significantly larger, depending on the degree and depth of N^2 variations at the polar summer mesopause (VF89).

Finally, turbulence typically survives for long times following its initiation. As examples, instabilities leading to turbulence have shear and buoyancy energy production terms that span several T_b (F09b), and $<\varepsilon>$ decreases by only ~3-4 times over the final 10 T_b of the PDFs shown in Fig. 14. While not a component of this study, KHI secondary instabilities and turbulence have comparable time scales for their evolutions (WF99; F12, F14b). Thus, successive, or unrelated, new GW or MSD instabilities have significant time over which to evolve prior to cessation of turbulence due to previous events.

Significant unknowns related to these studies at present include the following:

1) definition of the local environmental N needed to quantify estimates of S and ε,
2) influences of background turbulence, and a smaller "turbulent" Reynolds number, $Re_{turb}=\lambda_z^2/\nu_{turb}T_b$ (where $\nu_{turb}>\nu$ is the turbulent viscosity, F14b, F14c), on the character and intensities of new instabilities and turbulence, and
3) implications of DNS at lower Re than are realistic when background turbulence is weak.

Evidence for the influences of background turbulence on KHI seen in PMCs and OH airglow was provided in the studies by Baumgarten and Fritts (2014), F14b, Hecht et al. (2014), and F14c. In these cases, background $\nu_{turb}>\nu$ (and $Re_{turb}<Re$) were inferred due to larger observed spatial scales of secondary instabilities than were anticipated by DNS of KHI in the absence of an elevated viscosity. Estimates in these cases ranged from $\nu_{turb}\sim$5-40 ν (and $Re_{turb}\sim$0.025-0.2 Re), though much higher values are likely to accompany stronger turbulence sources. Assuming the same influences occur for other types of instabilities, we should expect our DNS of GW breaking and MSD to be appropriate for larger spatial scales that would otherwise have much higher Re. As an example, the GW breaking assumed to cause the vortex rings in Case 1 had

$Re=\lambda_z^2/\nu T_b$~8x10[5], assuming no turbulent viscosity. The Floquet theory for the DNS shown in Figs. 3 and 4 (F09a) suggests that a higher *Re* does not likely change the instability character, scales, or growth rates. However, larger ε accompany larger *Re* for the same underlying dynamics (F16). Hence smaller ν_{turb} and larger Re_{turb} would yield even larger ε estimates than discussed above.

Additional effects that accompany strong instabilities and turbulence in the MLT (and throughout the atmosphere) include local heating and turbulent mixing and transport. Turbulence heating rates are ~100 K/day for ε~1 Wkg^{-1} and thus comparable in magnitude to the adiabatic cooling driven by GW-induced upwelling near the polar summer mesopause. Turbulence is also anticipated by many to contribute a strong downward heat flux near and above the polar summer mesopause, but modeling of these dynamics has yet to confirm (or contradict) these expectations.

9. Summary and Conclusions

We have employed high-resolution DNS to explore the implications of instability features observed in high-resolution imaging of PMCs for turbulence sources and intensities near the polar summer mesopause. Imaging by ground-based cameras in Norway and serendipitously by star cameras as part of a cosmology experiment flown on a stratospheric balloon over Antarctica yielded evidence of various instability types suggesting idealized and multi-scale GW dynamics at PMC altitudes. Observations of instability features and scales enabled estimates of the underlying GW intrinsic properties and amplitudes in four cases.

Specific results and implications of our study include the following:

1) PMC imaging reveals an active dynamical environment with larger-scale GWs always present and smaller-scale instabilities occurring frequently, as also noted previously,
2) the dominant instabilities include KHI, GW breaking, and intrusions at multiple scales,
3) vortex rings are a frequent instability form accompanying GW breaking at various scales,
4) vortex rings occurring at large scales with close spacing imply large GW amplitude *a*, vertical wavelength λ_z, and intrinsic frequency ω_i, and large corresponding energy and momentum fluxes,

5) large GW $a=|u'/c_i|=|du'/dz|/N$~1, λ_z, and ω_i yield strong instabilities and turbulence,
6) MSD instabilities include local GW breaking, KHI, and intrusions, but these are often weaker and more challenging to quantify due to shallower instability depths,
7) while strong turbulence can arise rapidly (~1-2 T_b), turbulence decay can be very slow, e.g., a factor of ~3 or less over 10 T_b, and turbulence may thus persist for a long time,
8) estimates of $<\varepsilon>$ employing PMC imaging and numerical modeling are broadly consistent with the magnitudes inferred from *in-situ* measurements at the PMC altitudes.
9) larger ε within the modeled distributions also compared well with the larger measured values near the polar summer mesopause, where theory anticipates more continuous turbulence generation and larger magnitudes.

There remain uncertainties over the roles and implications of a turbulent viscosity, ν_{turb}, and an implied turbulent Reynolds number, Re_{turb}, in defining MLT instability dynamics, scales, and turbulence intensities. DNS of these dynamics appear to predict mean and maximum ε that agree reasonably with *in-situ* observations, despite having smaller than physical Re in the absence of background turbulence. Possible explanations are that pre-existing turbulence typically imposes a larger ν_{turb} and a smaller Re_{turb} or that $<\varepsilon>$ may be larger than measured because of the spatial intermittency of turbulence events, and strong turbulence within these events. Of these, the former appears to be more likely. The role of turbulence in heat and momentum transports is also unknown, but will likely need to rely on high-resolution DNS for its resolution.

Acknowledgments

Research described here was supported by NASA grants NNX16AF64G, NNX08AG40G, and NNX07AP36H and by NSF grants AGS-1136269, AGS-1445783, AGS-1510354, and AGS-1452183. This project has received funding from the European Union's Horizon 2020 research and innovation program under grant 653980/ARISEII. The authors gratefully acknowledge discussions of GW-driven PMC brightness variations with Amal Chandran and Gary Thomas and the use of the Werne/NWRA Triple Code for the simulations presented within. We also acknowledge the DoD High Performance Computing Modernization Program for access to supercomputer platforms that allowed the simulations reported here.

Case	**Event type**	λ_z **(km)**	a	ω_0 **(N)**	λ_h **(km)**	**C=λ_z^2/T_b^3**	$Re=\lambda_z^2/\nu T_b$	ε_{mean} **(Wkg^{-1})**	ε_{high} **(Wkg^{-1})**
1	ideal. GWB	>15	>1	>0.3		7.3	8.3x10^5	>0.55	>6
2	ideal. GWB	8-10	~1	>0.3		2.1-3.2	2.4-3.7x10^5	~0.06-0.25	~0.7-2.6
3	ideal. GWB	2	~1	>0.3		0.13	15,000	~0.004-0.01	~0.04-0.1
4	MSD GWB	1	>1			1.2	1.3x10^5	0.016	0.25

Table 1. GW parameters and ε estimates for idealized and MSD GW breaking (GWB) cases.

References

Achatz, U., 2005: On the role of optimal perturbations in the instability of monochromatic gravity waves, Phys. of Fluids, 17, 094107, doi:10.1063/1.2046709.

Achatz, U., 2007: The primary nonlinear dynamics of modal and nonmodal perturbations of monochromatic inertia-gravity waves, J. Atmos. Sci., 64, 74-95.

Andreassen, O., P. O. Hvidsten, D. C. Fritts, and S. Arendt, 1998: Vorticity dynamics in a breaking gravity wave, 1. Initial instability evolution, *J. Fluid Mech*., **367**, 27-46.

Balsley, B. B., and D. A. Carter, 1982: The spectrum of atmospheric velocity fluctuations at 8 and 86 km, Geophys. Res. Lett., 9, 465–468.

Balsley, B. B., R. G. Frehlich, M. L. Jensen, Y. Meillier, and A. Muschinski, 2003: Extreme gradients in the nocturnal boundary layer: Structure, evolution, and potential causes. J. Atmos. Sci., 60, 2496–2508.

Balsley, B. B., and R. Garello, 1985: The kinetic energy density in the troposphere, stratosphere, and mesosphere: A preliminary study using the Poker Flat MST radar in Alaska, Radio Sci., 20(6), 1355-1361.

Balsley, B. B., M. L. Jensen, and R. Frehlich, 1998: The Use of state-of-the-art kites for profiling the lower atmosphere, Bound. Layer Meteorol., 87, 1-25.

Balsley, B. B., D. A. Lawrence, R. F. Woodman, and D. C. Fritts, 2012: Fine-scale characteristics of temperature, wind, and turbulence in the lower atmosphere (0-1,300 m) over the south Peruvian coast, Bound. Layer Meteorol., DOI 10.1007/s10546-012-9774-x.

Baumgarten, G., A. Chandran, J. Fiedler, P. Hoffmann, N. Kaifler, J. Lumpe, A. Merkel, C. E. Randall, D. Rusch, and G. Thomas, 2012: On the horizontal and temporal structure of noctilucent clouds as observed by satellite and lidar at ALOMAR (69N), Geophys. Res. Lett., 39, L01803, doi:10.1029/2011GL049935.

Baumgarten, G., and D. C. Fritts, 2014: Quantifying Kelvin-Helmholtz instability dynamics observed in noctilucent clouds: 1. Methods and observations, J. Geophys. Res. Atmos., 119, 9324–9337, doi:10.1002/2014JD021832.

Chandran, A., D. W. Rusch, G. E. Thomas, S. E. Palo, G. Baumgarten, E. J. Jensen, and A. W. Merkel, 2012: Atmospheric gravity wave effects on polar mesospheric clouds: A comparison of numerical simulations from CARMA 2D with AIM observations, J. Geophys. Res., 117, D20104,doi:10.1029/2012JD017794.

Chuda, T., R. Kimura, and H. Niino, 2007: Vertical Fine Structures of Temperature and Water Vapor in the Free Atmosphere, J. Meteorol. Soc Japan, 85 (5), 583-597.

Clayson, C. A., and L. Kantha, 2008: On turbulence and mixing in the free atmosphere inferred from high-resolution soundings, J. Atmos. Ocean. Tech., 25, 833-852, DOI:10.1175/2007JTECHA992.1.

Coulman, C. E., J. Vernin, and A. Fuchs, 1995: Optical seeing mechanism of formation of thin turbulent laminae in the atmosphere, Appl. Opt., 34, 5461–5474, 1995.

Coy, L., and D. C. Fritts, 1988: Gravity wave heat fluxes: A Lagrangian approach, J. Atmos. Sci., 45, 1770-1780.

Dalaudier, F., C. Sidi, M. Crochet, and J. Vernin, 1994: Direct evidence of “sheets” in the atmospheric temperature field, J. Atmos. Sci., 51, 237–248.

Dillon, T. M., 1982: Vertical overturns: A comparison of Thorpe and Ozmidov length scales. J. Geophys. Res., 87, 9601–9613.

Dosser, H. V., and B. R. Sutherland, 2011: Weakly nonlinear non-Boussinesq internal gravity wavepackets, Physica D, 240, 346-356.

Engler, N., R. Latteck, B. Strelnikov, W. Singer, M. Rapp, 2005: Turbulent energy dissipation rates observed by Doppler MST Radar and by rocket-borne instruments during the MIDAS/MaCWAVE campaign 2002. Annales Geophysicae, European Geosciences Union, 23 (4), pp.1147-1156.

Ferron, B., H. Mercier, K. Speer, A. Gargett, and K. Polzin, 1998: Mixing in the Romanche fracture zone. J. Phys. Oceanogr., 28, 1929–1945.

Fritts, D. C., and M. J. Alexander, 2003: Gravity dynamics and effects in the middle atmosphere, Rev. Geophys., 41, doi:10.1029/2001RG000106.

Fritts, D. C., S. Arendt, and O. Andreassen, 1998: Vorticity dynamics in a breaking internal gravity wave, 2. Vortex interactions and transition to turbulence, J. Fluid Mech., 367, 47-65.

Fritts, D. C., G. Baumgarten, K. Wan, J. A. Werne, T. Lund, 2014b: Quantifying Kelvin-Helmholtz Instability Dynamics Observed in Noctilucent Clouds: 2. Modeling and Interpretation of Observations, J. Geophys. Res., 119 (15), 9324-9337.

Fritts, D. C., and T. J. Dunkerton, 1985: Fluxes of heat and constituents due to convectively unstable gravity waves, J. Atmos. Sci., 42 , 549-556.

Fritts, D. C., J. R. Isler, G. E. Thomas, and Ø. Andreassen, 1993: Wave breaking signatures in noctilucent clouds, Geophys. Res. Lett., 20, 2039–2042.

Fritts, D. C., B. Laughman, T. S. Lund, and J. B. Snively, 2015: Self-acceleration and instability of gravity wave packets: 1. Effects of temporal localization, J. Geophys. Res. Atmos., 120, 8783–8803, doi:10.1002/2015JD023363.

Fritts, D. C., P.-D. Pautet, K. Bossert, M. J. Taylor, B. P. Williams, H. Iimura, T. Yuan, N. J. Mitchell, and G. Stober, 2014a: Quantifying gravity wave momentum fluxes with Mesosphere Temperature Mappers and correlative instrumentation, J. Geophys. Res. Atmos., 119, 13,583–13,603, doi:10.1002/ 2014JD022150.

Fritts, D. C., K. Wan, J. Werne, T. Lund, and J. H. Hecht, 2014c: Modeling Influences of Kelvin-Helmholtz Instability Dynamics on Airglow, J. Geophys. Res., 119, 8858–8871, doi:10.1002/2014JD021737.

Fritts, D. C., and P. K. Rastogi, 1985: Convective and dynamical instabilities due to gravity wave motions in the lower and middle atmosphere: Theory and observations, Radio Sci., 20, 1247-1277.

Fritts, D. C., S. A. Vadas, and Y. Yamada, 2002: An estimate of strong local gravity wave body forcing based on OH airglow and meteor radar observations, Geophys. Res. Lett., 29 (10), 10.1029/2001GL013753.

Fritts, D. C., and T. E. VanZandt, 1993: Spectral estimates of gravity wave energy and momentum fluxes, I: Energy dissipation, acceleration, and constraints, J. Atmos. Sci., 50, 3685-3694.

Fritts, D. C., K. Wan, P. Franke, and T. Lund, 2012: Computation of clear-air radar backscatter from numerical simulations of turbulence, 3. Off-zenith measurements and biases throughout the lifecycle of a Kelvin-Helmholtz instability, J. Geophys. Res., 117, D17101, doi:10.1029/2011JD017179.

Fritts, D. C., and L. Wang, 2013: Gravity Wave – Fine Structure Interactions, Part 2: Energy dissipation evolutions, statistics, and implications, J. Atmos. Sci., 70, 3735-3755, DOI:10.1175/JAS-D-13-059.1.

Fritts, D. C., L. Wang, M. A. Geller, D. A. Lawrence, J. Werne, and B. B. Balsley, 2016: Numerical Modeling of Multi-Scale Dynamics at a High Reynolds Number: Instabilities, Turbulence, and an Assessment of Ozmidov and Thorpe Scales, J. Atmos. Sci., 73(2), 555-578, doi: 10.1175/JAS-D-14-0343.1.

Fritts, D. C., L. Wang, and J. Werne, 2013: Gravity Wave – Fine Structure Interactions, Part 1: Influences of fine structure form and orientation on flow evolution and instability, J. Atmos. Sci., 70, 3710-3733, DOI:10.1175/JAS-D-13-055.1.

Fritts, D. C., L. Wang, J. Werne, T. Lund, and K. Wan, 2009a: Gravity wave instability dynamics at high Reynolds numbers, 1: Wave field evolution at large amplitudes and high frequencies, J. Atmos. Sci., 66, 1126-1148, doi:10.1175/2008JAS2726.1.

Fritts, D. C., L. Wang, J. Werne, T. Lund, and K. Wan, 2009b: Gravity wave instability dynamics at high Reynolds numbers, 2: Turbulence evolution, structure, and anisotropy, J. Atmos. Sci., 66, 1149-1171, doi:10.1175/2008JAS2727.1.

Fritts, D. C., B. P. Williams, C.-Y. She, J. D. Vance, M. Rapp, F.-J. Lübken, F. J. Schmidlin, A. Müllemann, and R. A. Goldberg, 2004: Observations of extreme temperature and wind gradients near the summer mesopause during the MaCWAVE/MIDAS rocket campaign, Geophys. Res. Lett., 31, doi:10.1029/2003GL019389.

Fruman, M. D., Achatz, U., 2012: Secondary instabilities in breaking inertia-gravity waves., J. Atmos. Sci., 69, 303–322.

Fruman, M. D., S. Remmler, U. Achatz, and S. Hickel, 2014: On the construction of a direct numerical simulation of a breaking inertia-gravity wave in the upper mesosphere, J. Geophys. Res. Atmos., 119, 11,613–11,640, doi:10.1002/2014JD022046.

Gargett, A. E., 1999: Velcro measurements of turbulent kinetic energy dissipation rate. J. Atmos. Oceanic Technol., 16, 1973–1993.

Gossard, E. E., Gaynor, J. E., Zamora, R. J., and Neff, W. D., 1985: Fine structure of elevated stable layers observed by sounder and in-situ tower sensors, J. Atmos. Sci., 42, 2156–2169.

Hecht, J. H., 2004: Instability layers and airglow imaging, Rev. Geophys., 42, RG1001, doi:10.1029/2003RG000131.

Hecht, J. H., A. Z. Liu, R. L. Walterscheid and R. J. Rudy, 2005: Maui Mesosphere and lower thermosphere (Maui MALT) observations of the evolution of Kelvin-Helmholtz billows formed near 86 km altitude, J. Geophys. Res., 110, D09S10, doi:10.1029/2003JD003908.

Hecht, J. H., A. Z. Liu, R. L. Bishop, J. H. Clemmons, C. S. Gardner, M. F. Larsen, R. G. Roble, G. R. Swenson, and R. L. Walterscheid. 2004: An overview of observations of unstable layers during the Turbulent Oxygen Mixing Experiment (TOMEX), J. Geophys. Res., 109, D2, DOI: 10.1029/2002JD003123.

Hecht, J. H., K. Wan, L. J. Gelinas, D. C. Fritts, R. L. Walterscheid, S. J. Franke, G. R. Swenson, F. A. Vargas, A. Z. Liu, M. J. Taylor, and P.D. Pautet, 2014: The lifecycle of instability features measured from the Andes Lidar Observatory over Cerro Pachon on March 24, 2012, J. Geophys. Res., 119, 8872-8898, doi:10.1002/2014JD021726.

Lawrence, D. A., and B. B. Balsley, 2013: High-Resolution Atmospheric Sensing of Multiple Atmospheric Variables using the DataHawk Small Airborne Measurement System, J. Atmos. And Ocean. Tech., Vol. 30, 2352–2366, doi: http://dx.doi.org/10.1175/JTECH-D-12-00089.1

Lelong, M.-P., and T. J. Dunkerton, 1998a: Inertia–gravity wave breaking in three dimensions. Part I: Convectively stable waves. J. Atmos. Sci., 55, 2473–2488.

Lelong, M.-P., and T. J. Dunkerton, 1998b: Inertia–gravity wave breaking in three dimensions. Part II: Convectively unstable waves. J. Atmos. Sci., 55, 2489–2501.

Lehmacher, G. A., L. Guo, E. Kudeki, P. M. Reyes, A. Akgiray, and J. L. Chau, 2007: High-resolution observations of mesospheric layers with the Jicamarca VHF radar, Adv. Space Res., 40(6), 734-743.

Lehmacher, G. A., T. D. Scott, M. F. Larsen, S. G. Bilen, C. L. Croskey, J. D. Mitchell, M. Rapp, F.-J. Lübken, and R. L. Collins, 2011: The Turbopause experiment: Atmospheric stability and turbulent structure spanning the turbopause altitude, Ann. Geophys., 29, 2327-2339, doi:10.5194/angeo-29-2327-2011.

Lilly, D. K., 1983: Stratified turbulence and the mesoscale variability of the atmosphere, J. Atmos. Sci., 40, 749–761.

Lübken, F.-J., 1997: Seasonal variation of turbulent energy dissipation rates at high latitudes as determined by in situ measurements of neutral density fluctuations, J. Geophys. Res., 102, D12, 13,441-13,456.

Lübken, F.-J., M. Rapp, and P. Hoffmann, 2002: Neutral air turbulence and temperatures in the vicinity of polar mesosphere summer echoes, J. Geophys. Res., 107, 4273, doi:10.1029/2001JD000915.

Luce, H., M. Crochet, F. Dalaudier, and C. Sidi, 1995: Interpretation of VHF ST radar vertical echoes from in situ temperature sheet observations. Radio Sci., 30, 1002–1025.

Luce, H., Crochet, M., Hanuise, C., Yamamoto, M., and Fukao, S., On the interpretation of the layered structures detected by MST radars in dual Frequency Domain Interferometry (FDI) mode, Radio Sci., 34, 1077–1083, 1999.

Luce, H., G. Hassenpflug, M. Yamamoto, and S. Fukao, 2006: High-resolution vertical imaging of the troposphere and loer stratosphere using the new MU radar system, Ann. Geophys., 24, 791-805, www.ann-geophys.net/24/791/2006.

McIntyre, M. E., 1989: On dynamics and transport near the polar mesopause in summer, J. Geophys. Res., 94(D12), 14,617-14,628.

Moum, J. N., 1996: Energy-containing scales of turbulence in the ocean thermocline. J. Geophys. Res., 101, 14 095–14 101.

Muschinski, A., and C. Wode, 1998: First in situ evidence for coexisting submeter temperature and humidity sheets in the lower free troposphere. J. Atmos. Sci., 55, 2893–2906.

Nastrom, G. D., and F. D. Eaton, 2001: Persistent layers of enhanced Cn2 in the lower stratosphere from radar. Radio Sci., 36, 137–149.

Osborn, T. R., 1980: Estimates of the local rate of vertical diffusion from dissipation measurements. J. Phys. Oceanogr., 10, 83–89.

Osborn, T. R., and Cox, 1972: Oceanic fine structure, Geophys. Fluid Dyn., 3(1), 321-345, DOI:10.1080/03091927208236085.

Pfrommer, T., P. Hickson, and C.-Y. She, 2009: A large-aperture sodium fluorescence lidar with very high resolution for mesopause dynamics and adaptive optics studies, Geophys. Res. Lett., 35(15), L15831, DOI: 10.1029/2009GL038802.

Rapp, M., B. Strelnikov, A. Müllemann, F.-J. Lübken, and D. C. Fritts, 2004: Turbulence measurements implications for gravity wave dissipation during the MaCWAVE/MIDAS summer rocket program, Geophys. Res. Lett., 31, doi:10.1029/2003GL019325.

Remmler, S., Fruman, M. D., Hickel, S., 2013: Direct numerical simulation of a breaking inertia-gravity wave., J. Fluid Mech., 722, 424–436.

Sato, T., and R. F. Woodman, 1982: Fine altitude resolution radar observations of stratospheric turbulent layers by the Arecibo 430 MHz radar, J. Atmos. Sci., 39, 2546–2552.

Schneider, A., M. Gerding, and F.-J. Lübken, 2014: Comparing turbulent parameters obtained from LITOS and radiosonde measurements, Atmos. Chem. Phys. Discussion, 14, 19033-19053, doi:10.5194/acpd-14-19033-2014.

Smyth, W. D., and J. N. Moum, 2000: Length scales of turbulence in stably stratified mixing layers. Phys. Fluids, 12, 1327–1342.

Strelnikov, B., M. Rapp, I. Strelnikova, N. Engler, and R. Latteck, 2009: Small-scale structures in neutrals and charged aerosol particles as observed during the ECOMA/MASS rocket campaign, Ann. Geophys., 27, 1449-1456, www.ann-geophys.net/27/1449/2009.

Sutherland, B. R., 2001: Finite-amplitude internal wavepacket dispersion and breaking, J. Fluid Mech, 429, 343–380.

Sutherland, B. R., 2006b: Weakly nonlinear internal gravity wavepackets, J. Fluid Mech., 569, 249–258.

Sutherland, B. R., 2006a: Internal wave instability: Wave-wave versus wave-induced mean flow interactions, Phys. Fluids 18, 074107, doi:10.1063/1.2219102.

Thorpe, S. A., 1977: Turbulence and mixing in a Scottish loch, Philos. Trans. Roy. Soc. Lon., A286, 125–181.

Thorpe, S. A., 1999: On the breaking of internal waves in the ocean, J. Phys. Ocean., 29, 2433-2441

Thorpe, S. A., 2005: The Turbulent Ocean, Cambridge Univ. Press, Cambridge, U. K.

Walterscheid, R. L., 1981: Inertio-gravity wave induced accelerations of mean flow having an imposed periodic component: Implications for tidal observations in the meteor region, J. Geophys. Res., 86, 9698–9706.

Werne, J., and D. C. Fritts, 1999: Stratified shear turbulence: Evolution and statistics, Geophys. Res. Lett., 26, 439-442.

Wesson, J. C., and M. C. Gregg, 1994: Mixing in the Camarinal Sill in the Strait of Gibraltar. J. Geophys. Res., 99, 9847–9878.

Witt G., 1962: Height, structure and displacements of noctilucent clouds, Tellus 14, 1-18.

Woodman, R. F., and A. Guillen, 1974: Radar Observations of Winds and Turbulence in the Stratosphere and Mesosphere. Journal of the Atmospheric Sciences, 31, 493–505, doi: 10.1175/1520-0469(1974)031<0493:ROOWAT>2.0.CO;2.

Woods, J. D. and R. L. Wiley, 1972: Billow turbulence and ocean microstructure, Deep Sea Res., 19, 87–121.

Yamada, Y., H. Fukunishi, T. Nakamura, and T. Tsuda, 2001: Breakdown of small-scale quasi-stationary gravity wave and transition to turbulence observed in OH airglow, Geophys. Res. Lett., 28, 2153-2156.

Figures

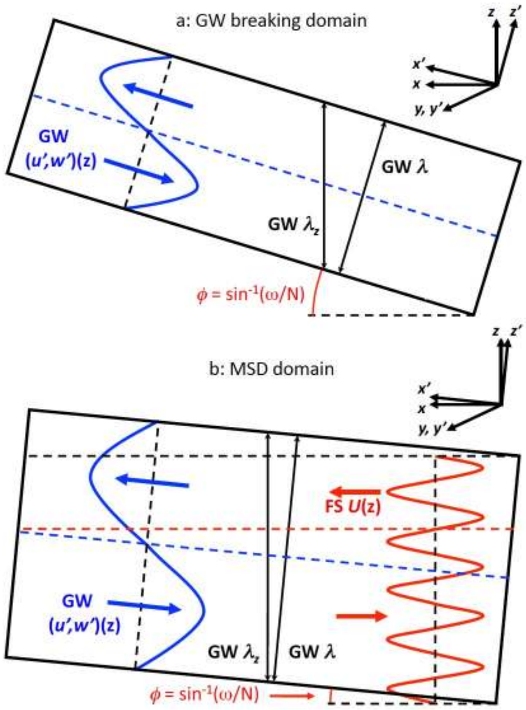

Figure 1. Tilted computational domains aligned along the primary GW for (a) the idealized DNS of GW breaking for *a*=0.9 and 1.1 and (b) the MSD DNS of a superposed initial GW and mean small-scale shear flow. The domain and geophysical coordinates are (*x'*,*y'*,*z'*) and (*x*,*y*,*z*) in each case and blue and red arrows and oscillatory curves show the initial GW and mean shear flows. See text for additional details on other initial conditions and flow parameters.

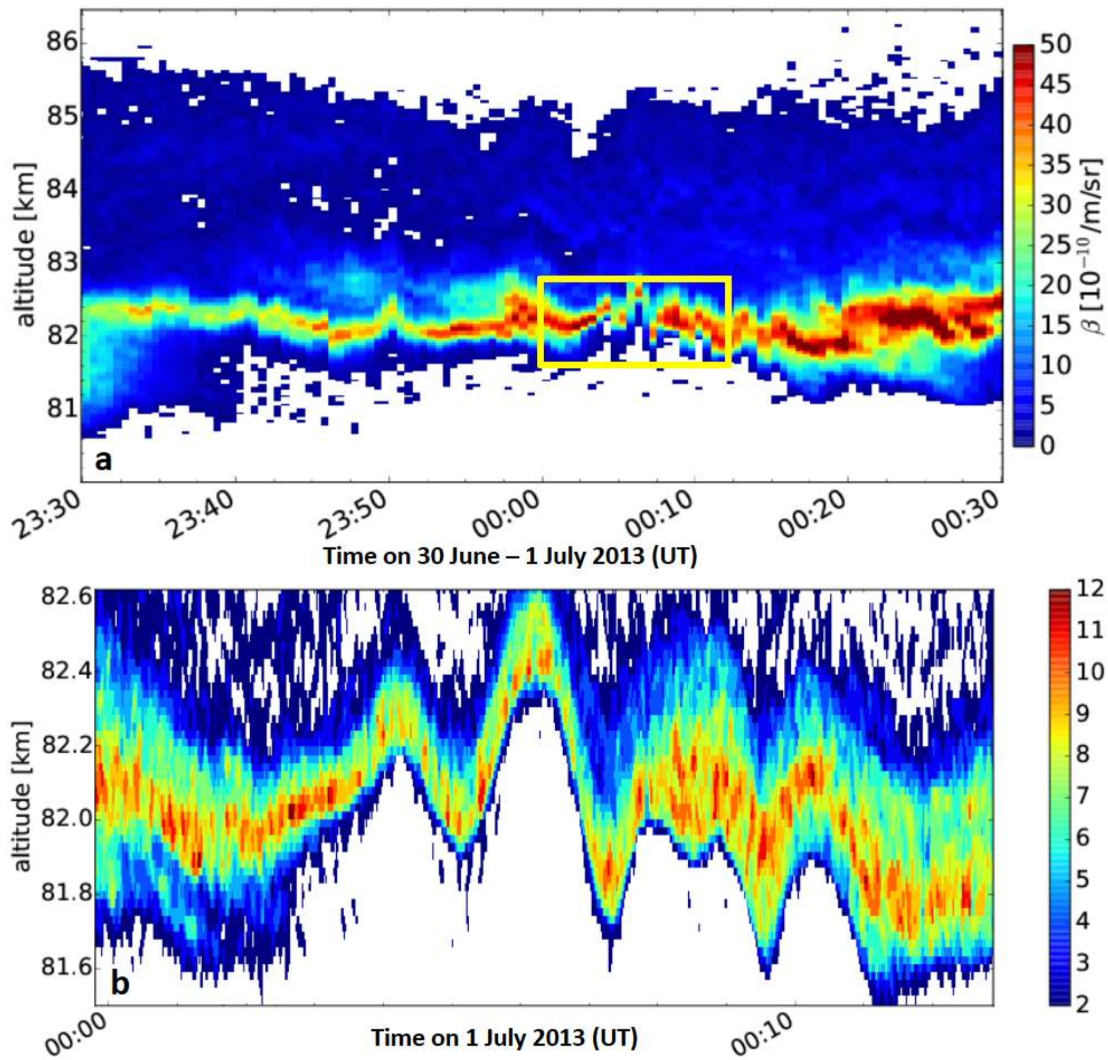

Figure 2. Measurements of PMC layer thickness with the Rayleigh-Mie-Raman lidar at ALOMAR from (a) 23:30-00:30 UT on 30 June to 1 July 2013 and (b) 00:00-00:12 UT on 1 July 2013. The times and altitudes shown in (b) are highlighted in the yellow rectangle in (a). Note that the layer FWHM can often be <100 m.

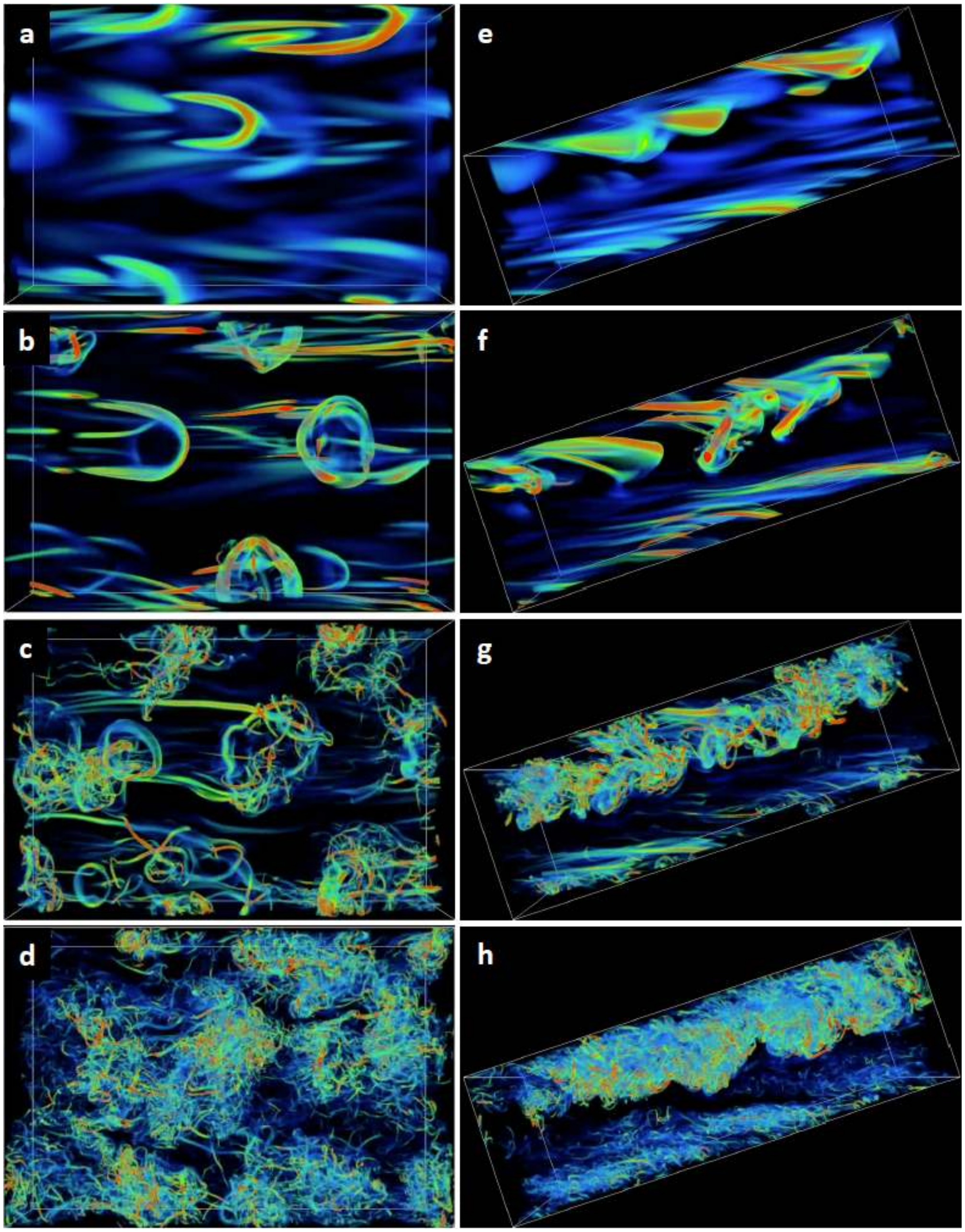

Figure 3. 3D volumetric views of λ_2 from (a-d) below and (e-h) the side showing the evolution of initial instabilities and turbulence accompanying the GW breaking DNS with *a*=0.9 at 21, 22, 23, and 24 T_b (top to bottom). The GW is shown propagating upward and to the right for more convenient comparisons with the PMC imaging from the ground. The color scale varies from weak (light blue) to intense (yellow/red) rotation.

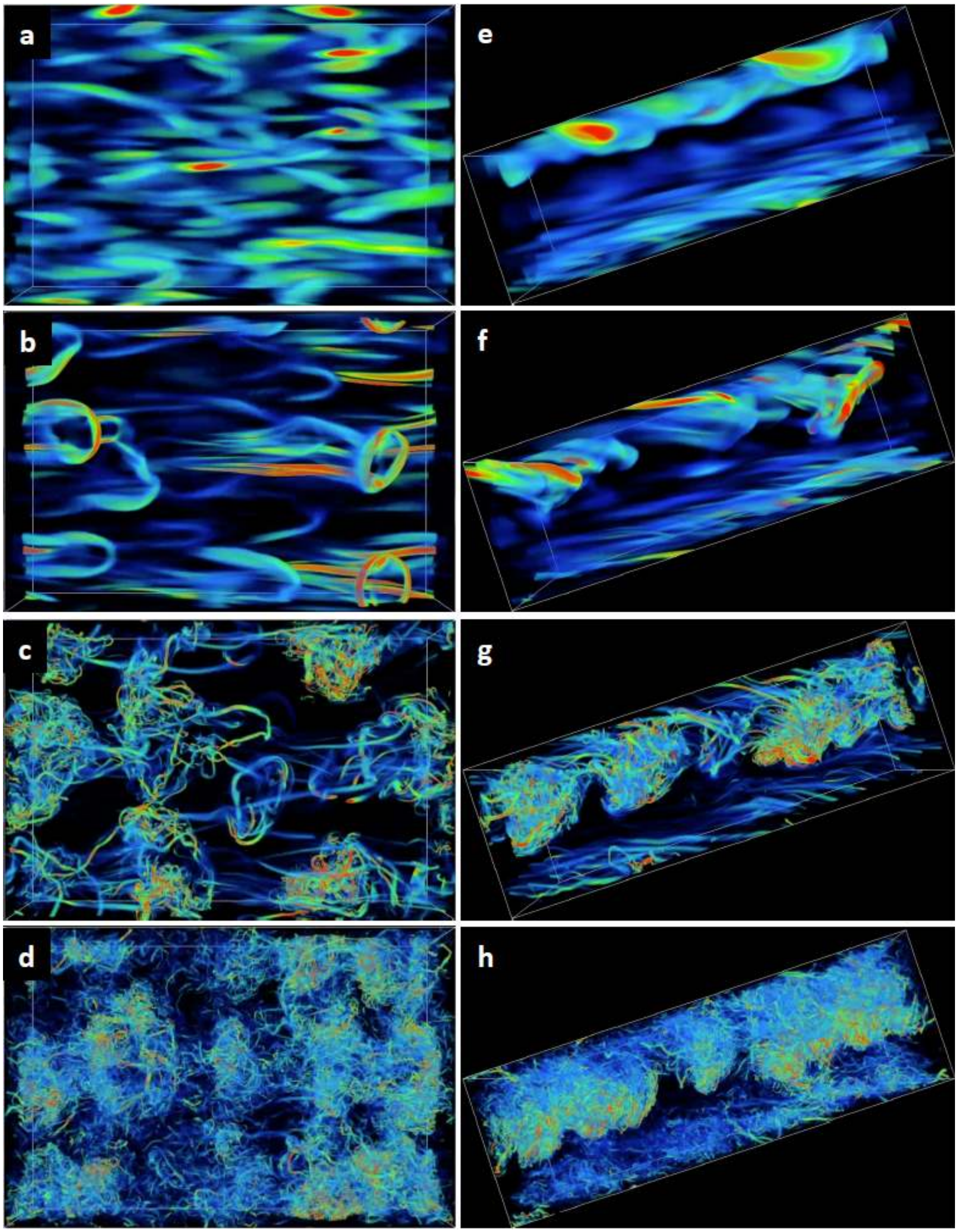

Figure 4. As in Fig. 3 for the GW breaking DNS with a=1.1 at 9.2, 10.2, 11.2, and 12.2 T_b.

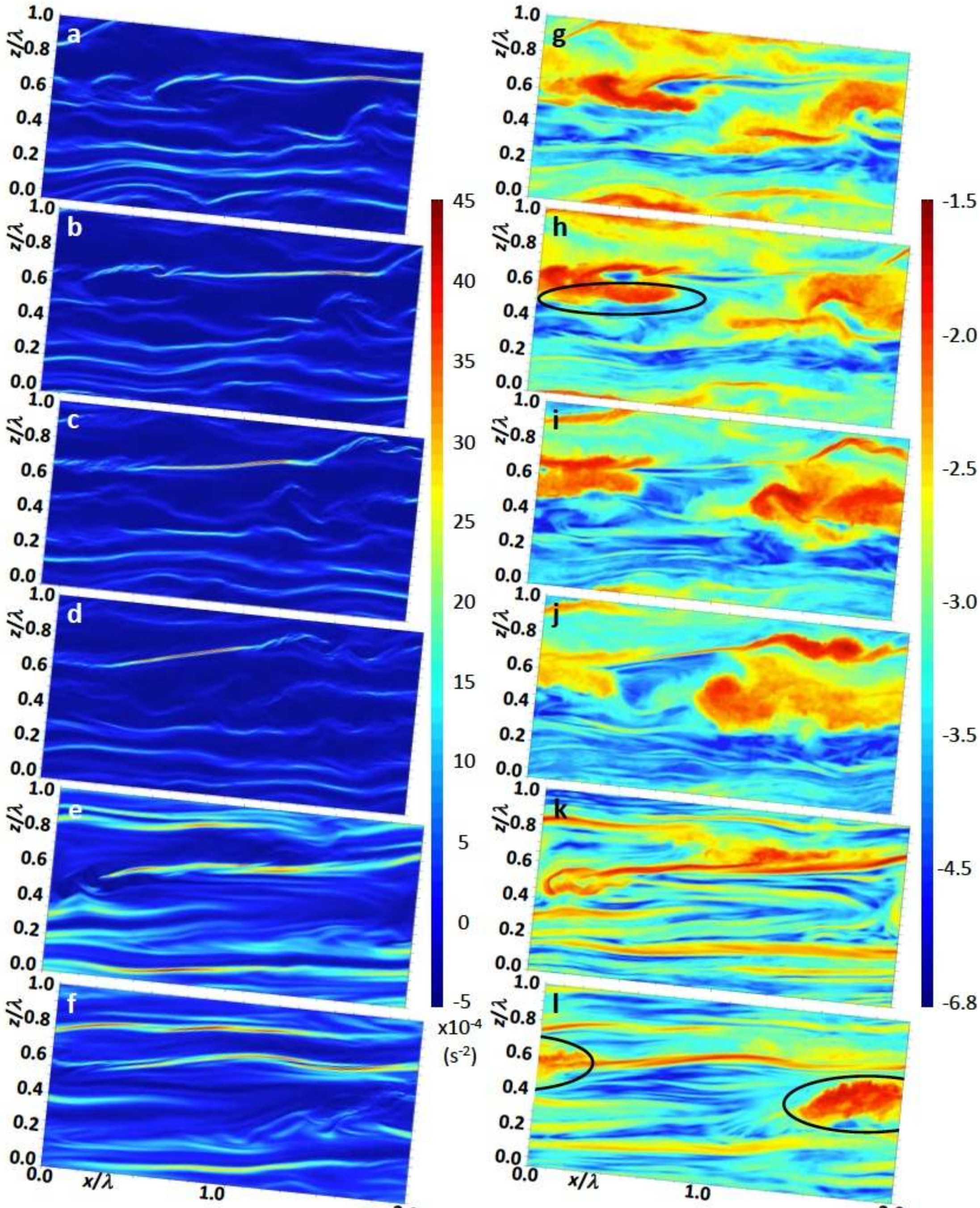

Figure 5. Spanwise-averaged $N^2(x,z)$ and $\log_{10}\varepsilon(x,z)$ for the MSD DNS described in Section 4.2 showing an evolving GW breaking and KHI at 10, 10.4, 11, and 11.6 T_b (a-d and g-j) and an intrusion event at 31.7 and 33 T_b (e and f, k and l). The N^2 color scale has a maximum of ~11 N_0^2 and the $\log_{10}\varepsilon(x,z)$ color scale is nondimensional and must be scaled by $S=\lambda_z^2/T_b^3$.

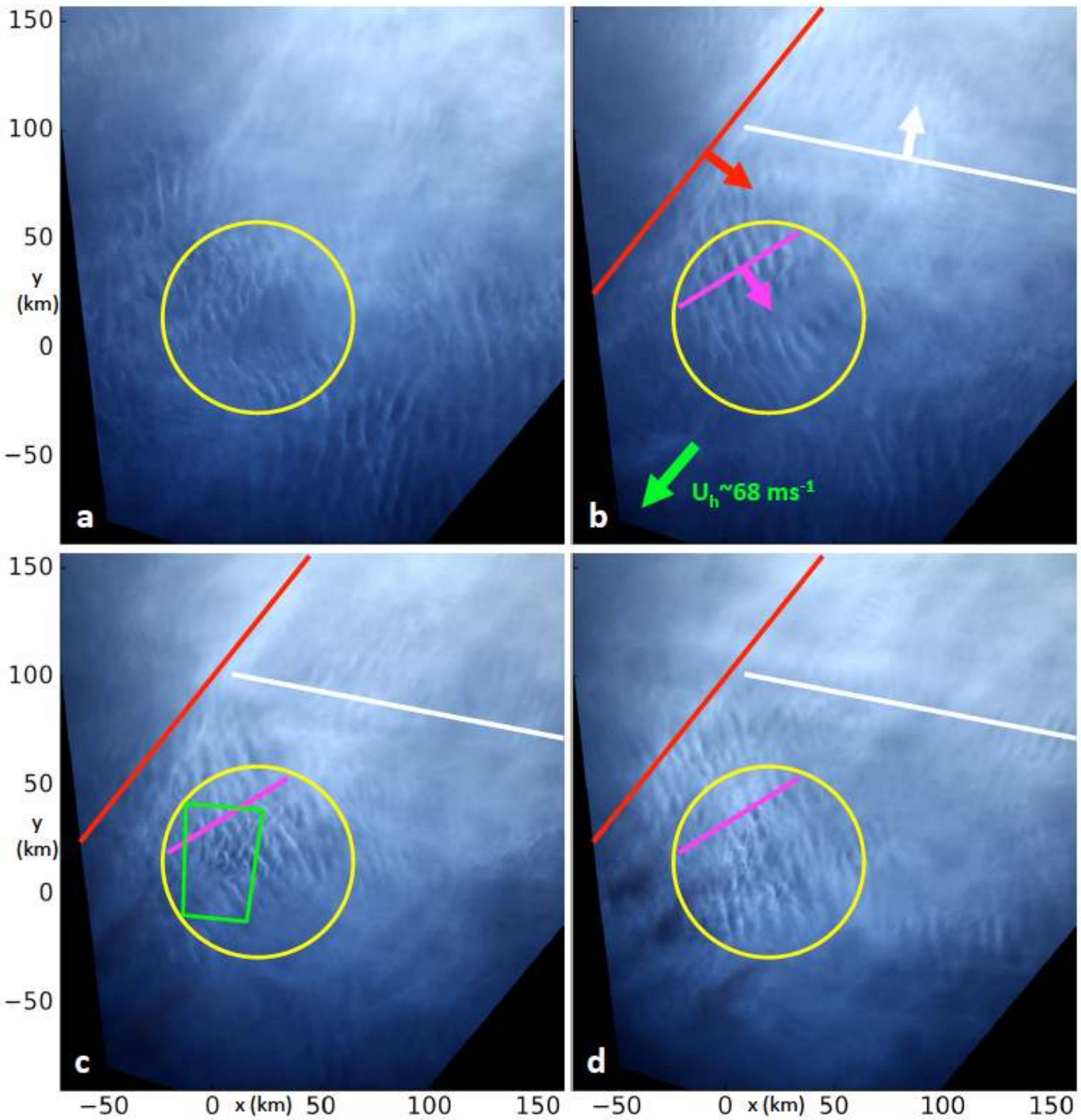

Figure 6. Ground-based wide-FOV PMC images viewing NNE from Trondheim, Norway on 1 August 2009 at 23:20, 23:30, 23:40, and 23:50 UT (a-d). The images are projected to the PMC altitude of ~82 km viewed from above, with N and E up and to the right. The FOV spans >200x200 km, yellow circles highlight the GW instability event of interest, the green trapezoid in (c) indicates the narrower FOV employed to examine the GW instability structures, and the lines and corresponding arrows show the phase orientations and propagation directions of the primary GWs.

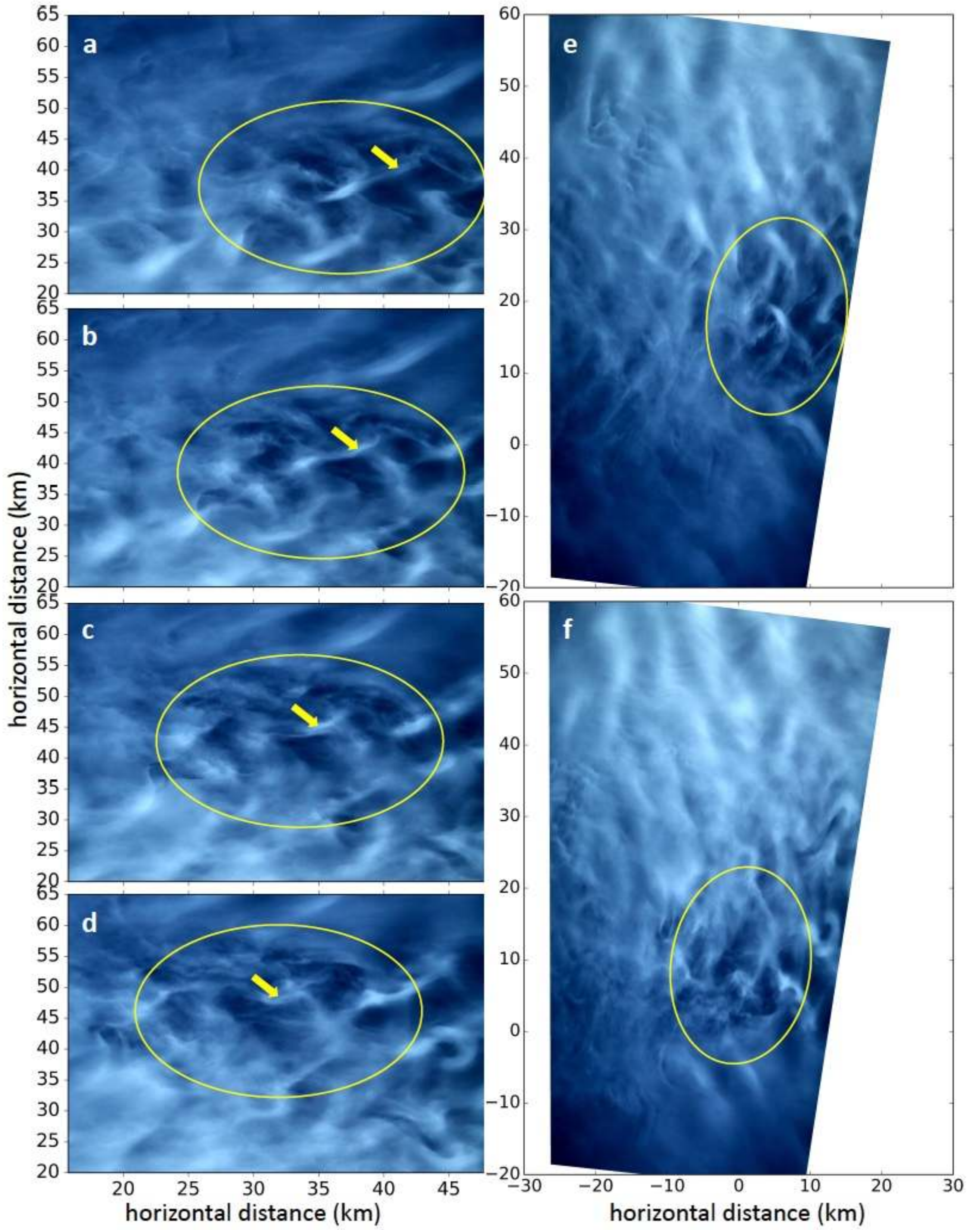

Figure 7. Narrow FOV images of the GW breaking event showing the evolutions of vortex rings from 23:42-23:45 UT (a-d) at a slant angle of ~21^{o} below the horizontal and ahead and to the right of the GW propagation direction (towards the SE). Yellow ovals highlight the major vortex rings occurring during this phase of the event; yellow arrows show the motion of the trailing vortices for the most upstream (eastward vortex ring). Panels (e) and (f) show the projected fields in (a) and (d).

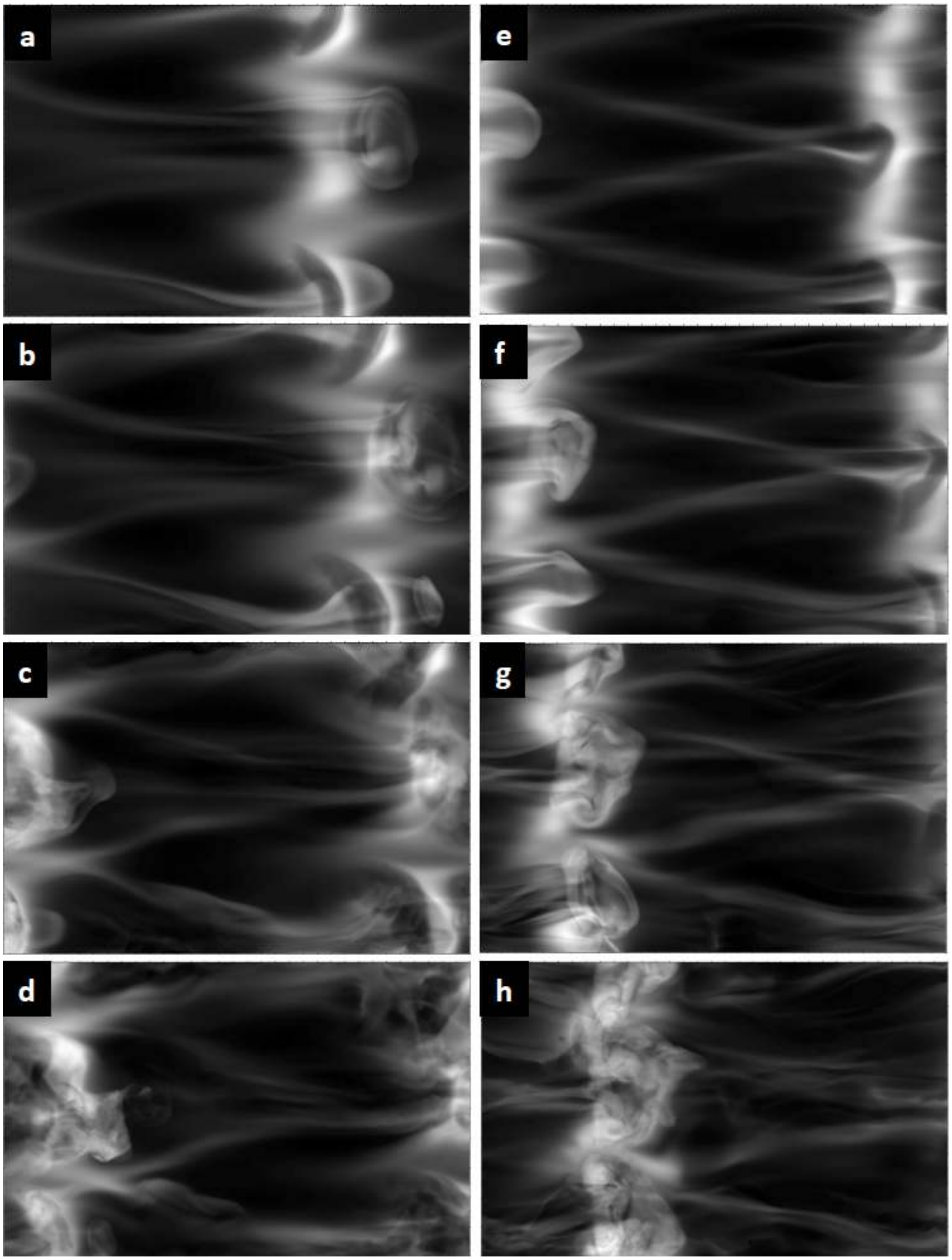

Figure 8. Simulated PMC responses in the GW breaking DNS for a=0.9 from 22-23 (a-d) T_b and for a=1.1 from 10.2-11.2 (e-h) at ~0.33 T_b intervals having a PMC layer centered on the vortex rings in the most unstable phase of the GW with z_{FWHM}=0.1 λ_z in each case.

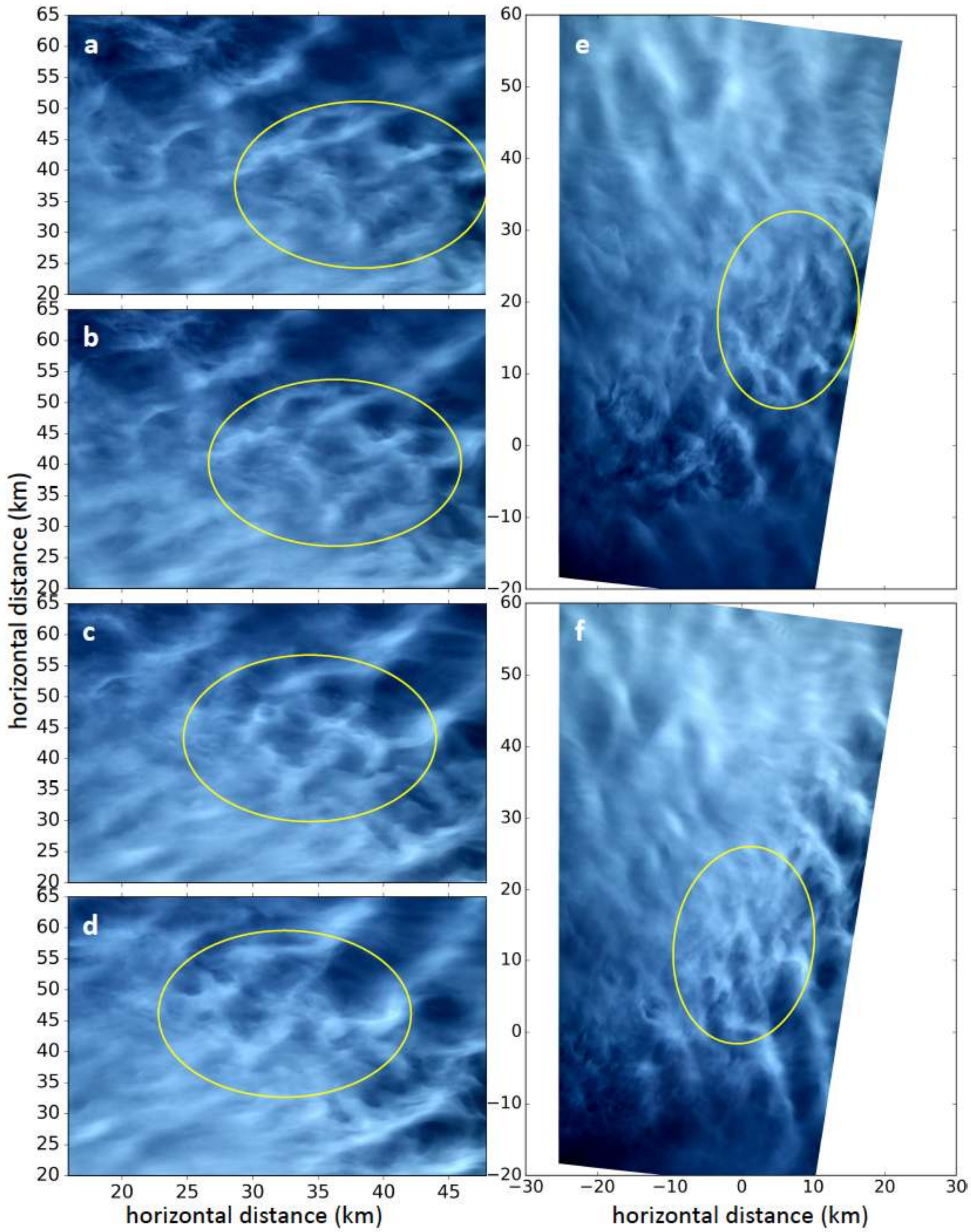

1089 **Figure 9.** As in Fig. 7 for 23:47-23:50 UT. The yellow ovals in this case show new vortex rings

1090 that formed to the SE of those shown in Fig. 7.

1091

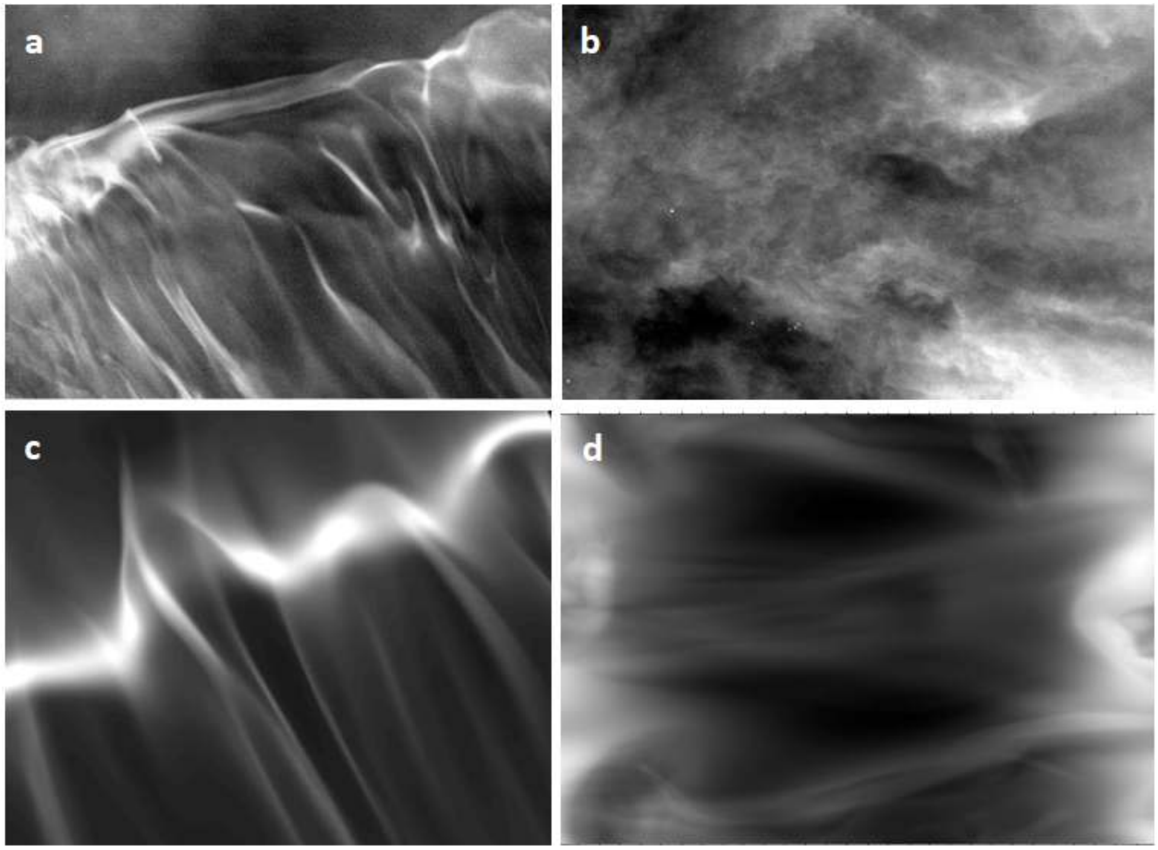

Figure 10. PMC imaging by the EBEX star cameras showing a GW breaking front (a) and a zig-zag pattern at the time of initial streamwise vortex generation (b) in projected FOVs of 4.4x3.9 km. Panels (c) and (d) show corresponding images of simulated PMCs with z_{FWHM}=100 m from the GW breaking DNS shown in Fig. 4 at 10.25 T_b and Fig. 3 at ~22 T_b, respectively.

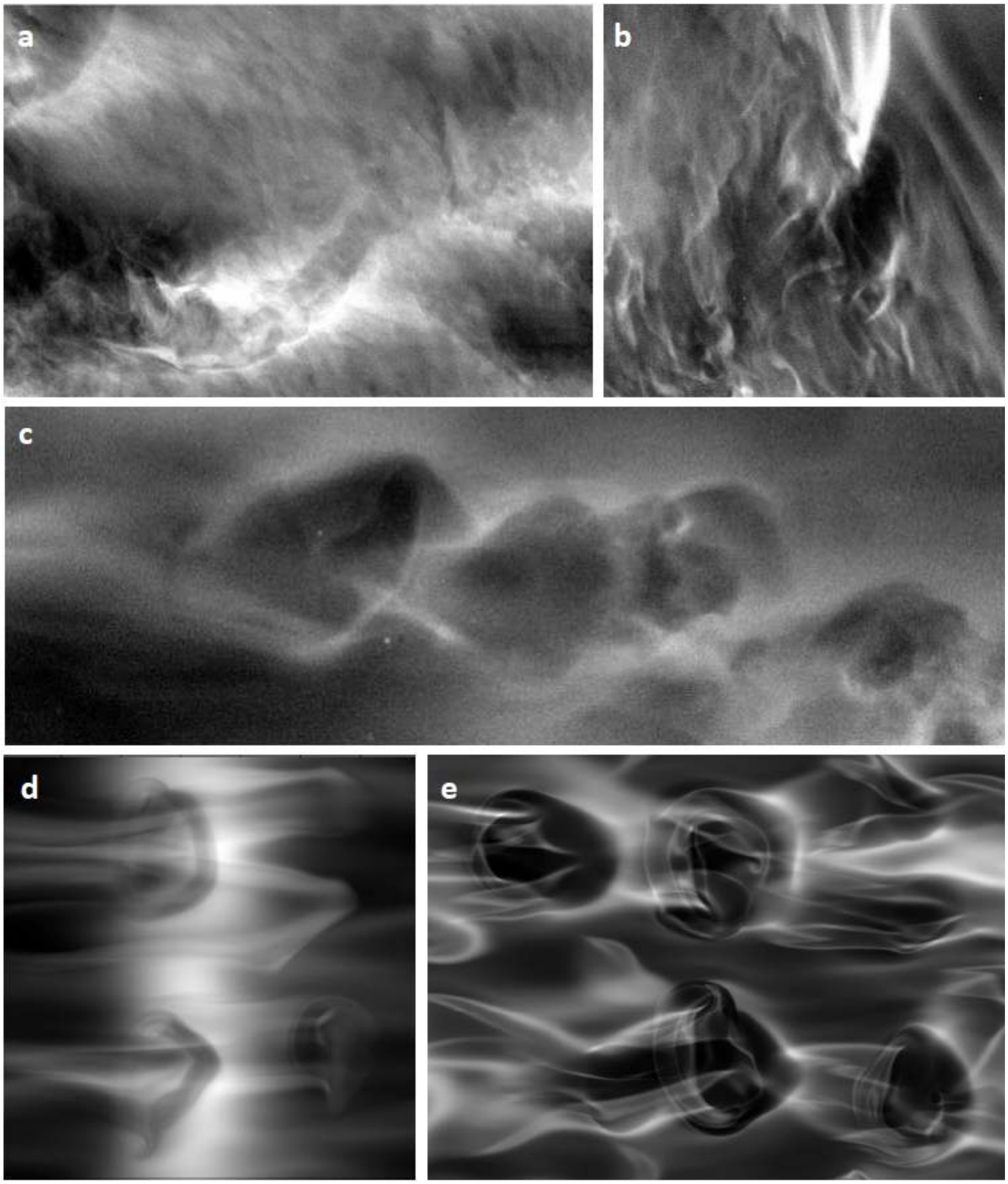

Figure 11. As in Fig. 10 showing PMC images of vortex rings at various scales, orientations, and evolution stages (a-c). PMC image FOVs are 4.4x3.9, 4x3.9, and 4.4x2 km, respectively. Panels (d) and (e) show two images of vortex rings from the GW breaking DNS for a=1.1 at ~10.5 T_b with z_{FWHM}=0.2 λ_z at the level of the vortex rings (d) and with z_{FWHM}=0.05 λ_z somewhat above.

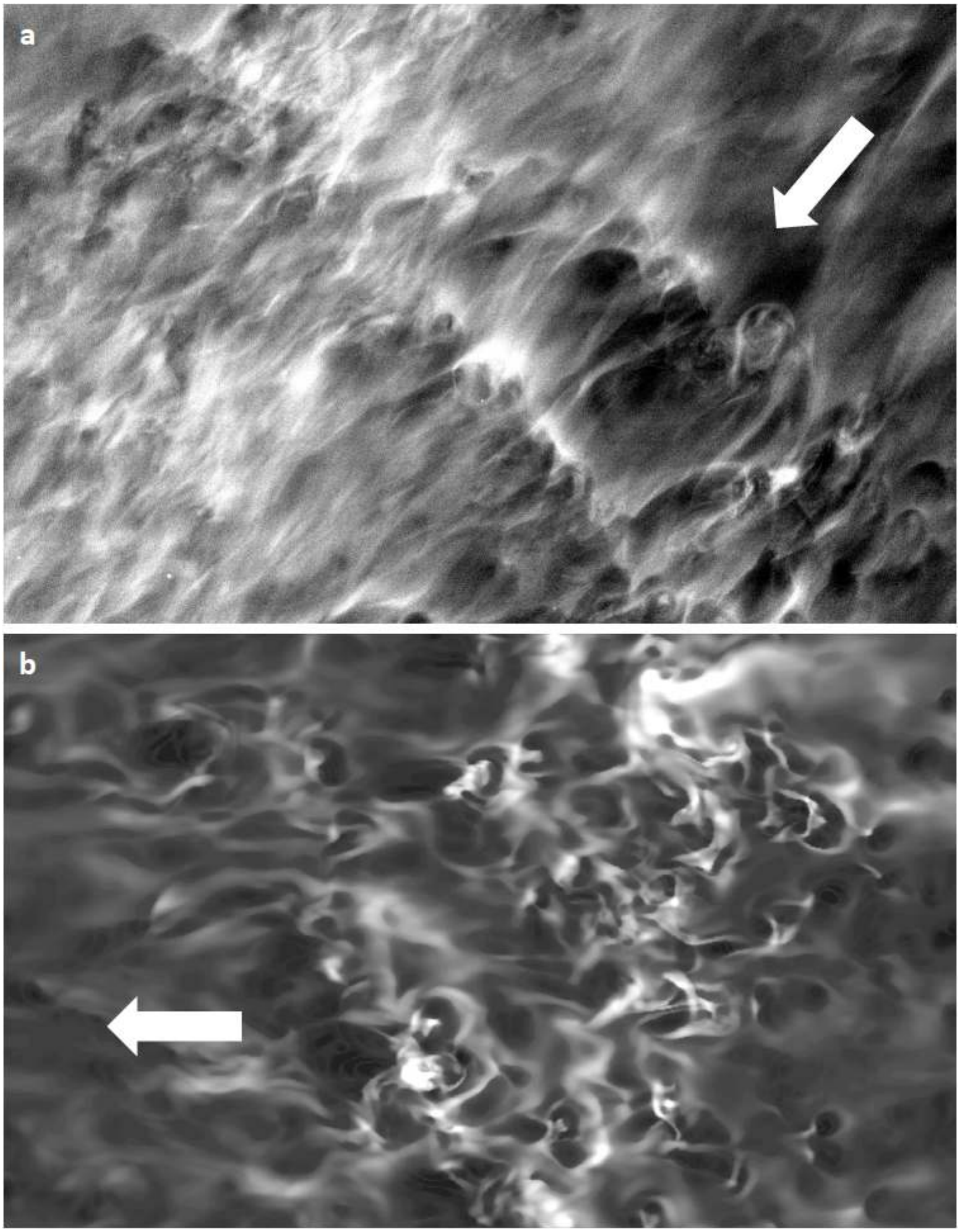

Figure 12. As in Fig. 10 showing a PMC image of cusp-like structures below an apparent region of local GW breaking in an MSD environment (a) and a simulation of similar features from a DNS of an MSD flow (b). The projected FOV of the PMC image in (a) is 4.4x3.9 km. The MSD dynamics occur in the black oval in Fig. 5h. Arrows in each panel show the direction of shearing below these structures.

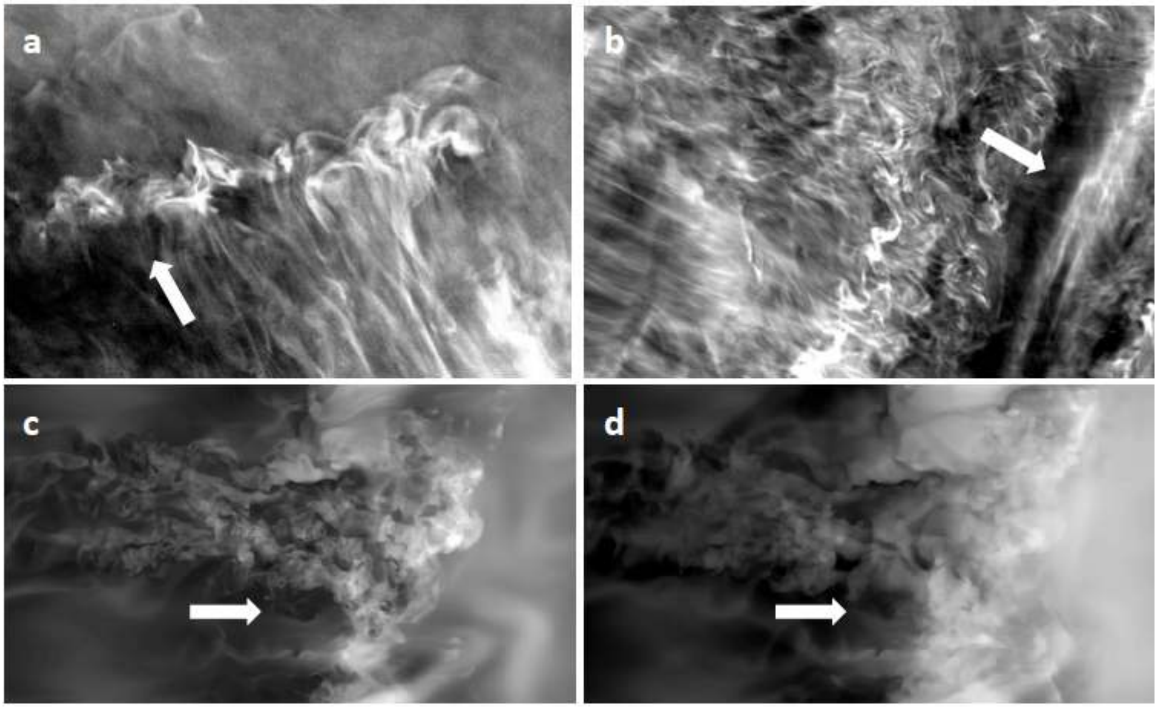

Figure 13. As in Fig. 12 showing PMC images of apparent intrusions (a and b) in projected FOVs of 3.7x2.6 and 4.4x3.9 km, respectively. Panels (c) and (d) show a simulated PMC arising from the intrusion in the black oval in Fig. 5h with z_{FWHM}=100 and 300 m (c and d) to illustrate the increased sensitivity to small-scale features by a thinner PMC layer.

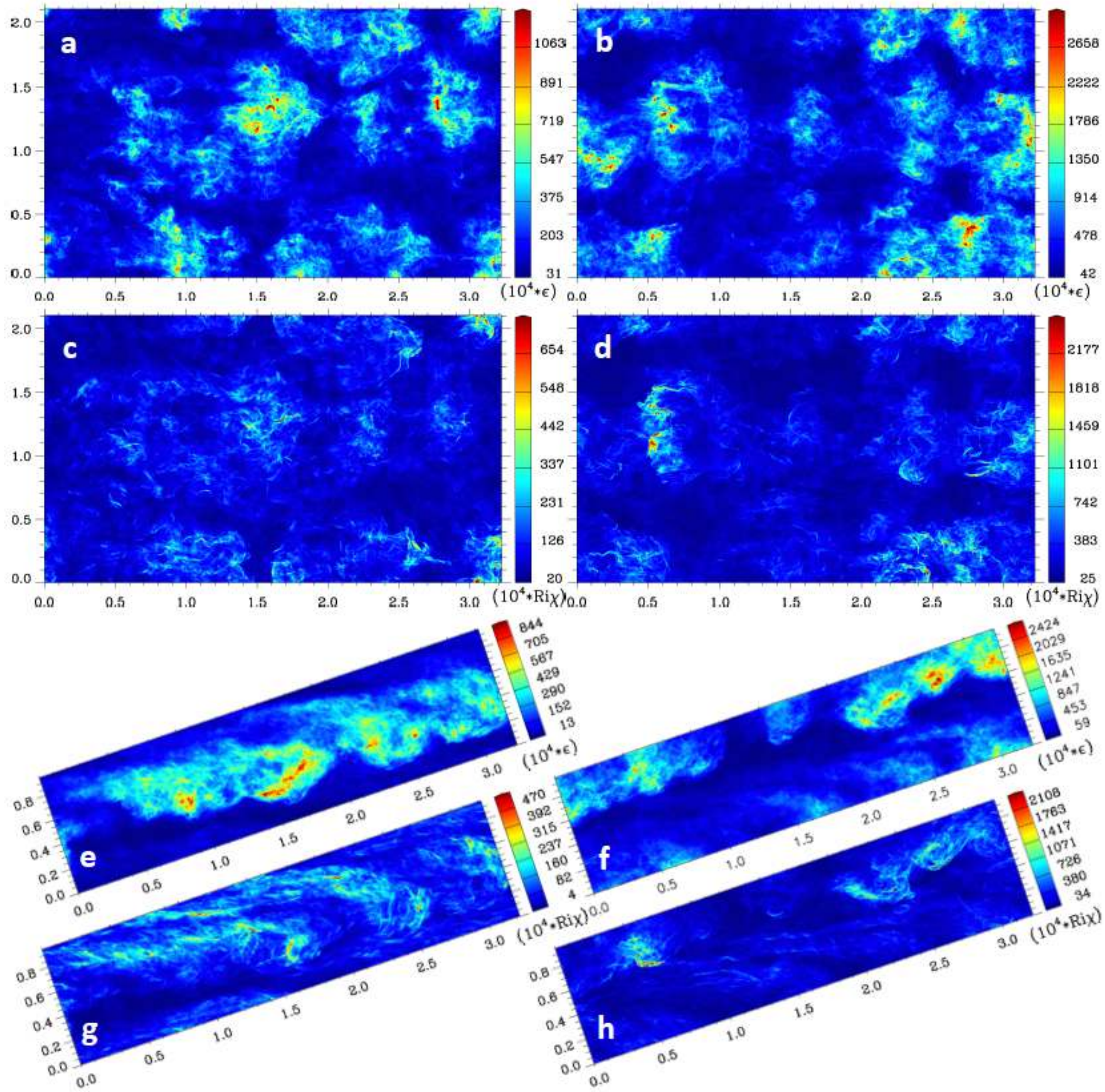

Figure 14. Horizontal (top panels) and vertical (bottom panels) cross sections of vertically- and spanwise-averaged (top and bottom, respectively) ε and the thermal energy dissipation rate, $Ri\chi$, for the DNS of GW breaking shown in Figs. 3 and 4. ε cross sections are shown in panels (a) and (e) for a=0.9 and in panels (b) and (f) for a=1.1. Corresponding $Ri\chi$ cross sections are shown in panels (c), (d), (g), and (h). Note that due to the vertical and spanwise averaging of ε and $Ri\chi$, the ranges of values in the color scales are now ~2 rather than ~4 decades in each case. The color bars also have upper limits at the magnitude above while 0.1% of ε and $Ri\chi$ occur.

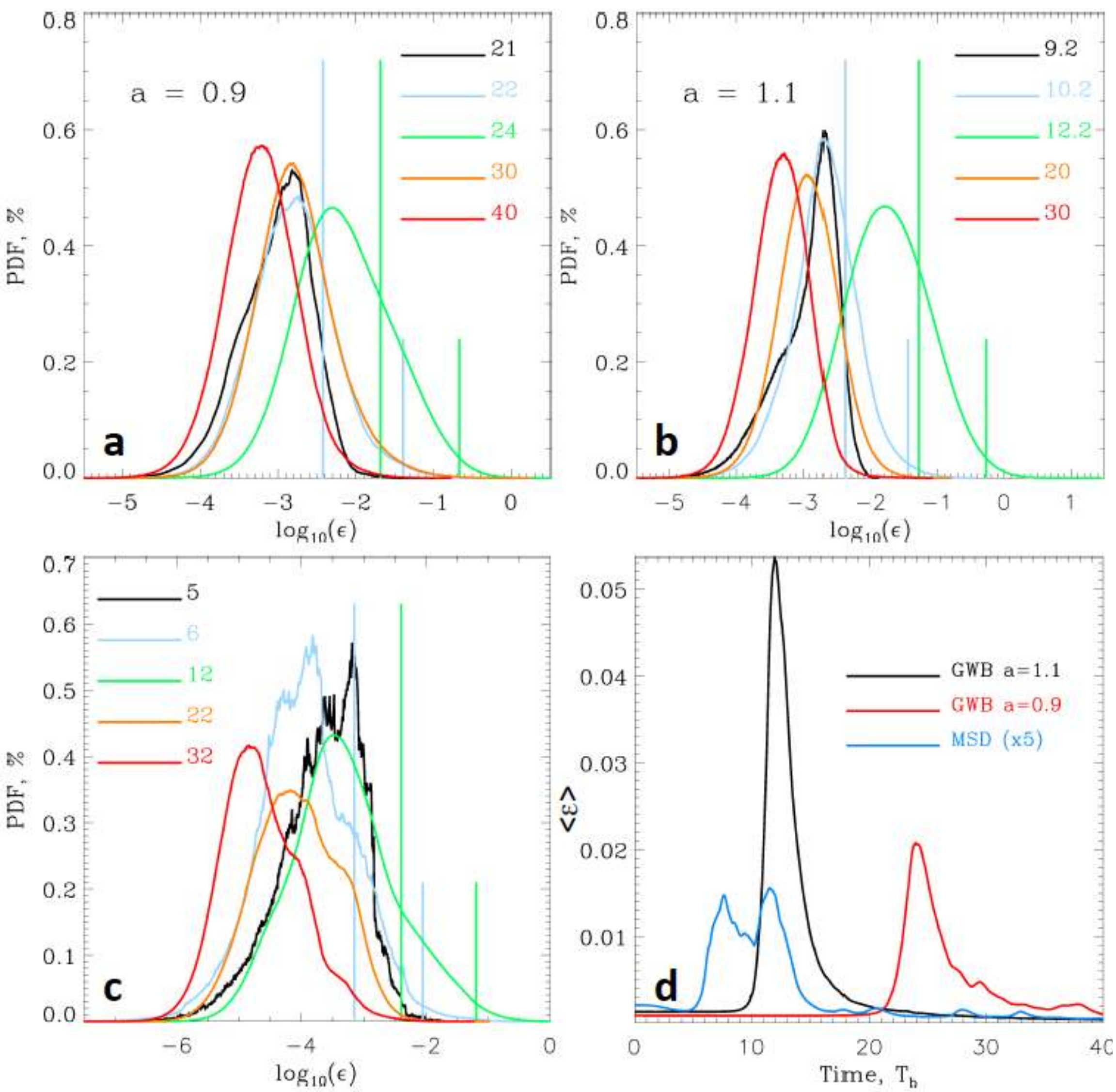

Figure 15. PDFs of $\log_{10}\varepsilon$ for GW breaking with a=0.9 and a=1.1, and for the MSD DNS are shown in (a-c), respectively. Times shown in each panel extend from initial instability stages to late in the turbulence decay. Vertical lines for the second and third times in each case show $\langle\varepsilon\rangle$ and ε_{high}. Nondimensional domain-mean ε are shown from 0-40 T_b for the three DNS in panel (d). Note that turbulence intensities are very much smaller for the MSD than for the GW breaking cases for the same domain depths.

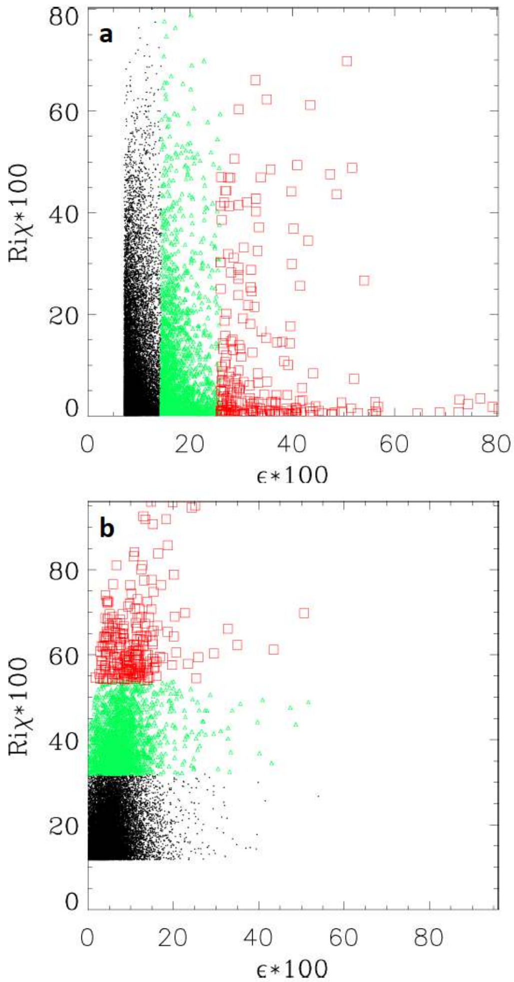

Figure 16. Comparisons of the relative values of ε and $Ri\chi$ for the largest values of ε (a) and $Ri\chi$ (b) averaged over 64 grid points. In each case, red squares, green triangles, and black dots denote values of ε (a) or $Ri\chi$ (b) among the largest 0.1-0.01%, 0.01-0.001%, and above 0.001%, respectively.